

1991

Differential heterodyne polarimetric sensor using a surface acoustic wave optical frequency shifter

Michael N. Trainer
Lehigh University

Follow this and additional works at: <https://preserve.lehigh.edu/etd>

 Part of the [Electrical and Computer Engineering Commons](#)

Recommended Citation

Trainer, Michael N., "Differential heterodyne polarimetric sensor using a surface acoustic wave optical frequency shifter" (1991).
Theses and Dissertations. 5524.
<https://preserve.lehigh.edu/etd/5524>

This Thesis is brought to you for free and open access by Lehigh Preserve. It has been accepted for inclusion in Theses and Dissertations by an authorized administrator of Lehigh Preserve. For more information, please contact preserve@lehigh.edu.

Differential Heterodyne Polarimetric Sensor
using a Surface Acoustic Wave Optical Frequency Shifter

by

Michael N. Trainer

A Thesis

Presented to the Graduate Committee

of Lehigh University

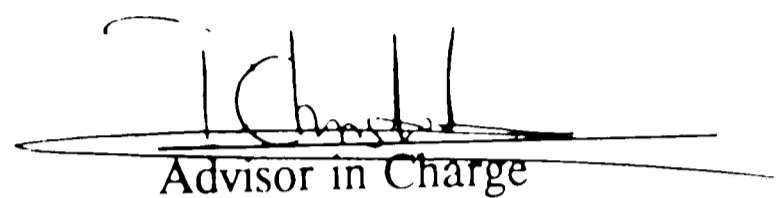
in Candidacy for the Degree of
Master of Science

in

Electrical Engineering

This thesis is accepted and approved in partial fulfillment of the requirements for the degree of Master of Science in Electrical Engineering.

Aug 21, 1991
Date


Advisor in Charge


CSEE Department Chairperson

Acknowledgements

I would like to acknowledge Spenser Silverthorne's contribution to the photolithography of the surface acoustic wave device.

Table of Contents

	Page
1 Abstract	1
2 Introduction	2
3 Elastooptic effect	4
4 Differential heterodyne	7
5 Frequency shifting devices	11
6 Surface acoustic wave frequency shifter	14
7 Surface acoustic waves	21
8 Polarization analysis	32
9 Noise and optical coherence	39
10 Experimental system design	46
11 Differential phase experiments	53
12 Conclusion	58
13 List of references	59
14 Appendix A	62
15 Appendix B	63
16 Vita	64

List of Figures

Figure		Page
1	Fiber optic sensor	3
2	Differential heterodyne polarimetric sensor system	9
3	Polarization intensities I_x and I_y vs. distance parameter AZ/π for $\Delta k=2A$	20
4	Diagram of surface acoustic wave device	22
5	Mode coupling efficiency vs. fiber angle θ	24
6	Mode coupling efficiency vs. acoustic frequency at optimum fiber angle θ	25
7	Delta function model for interdigitated SAW device	26
8	Mode coupling efficiency vs. acoustic frequency including SAW frequency response at $\Delta k=0$	28
9	Equivalent circuit of interdigitated SAW device	29
10	Definitions of polarization axis orientations at various points in the optical system	32
11	Electric field vector diagram at the sensor output polarizer	36
12	Experimental system diagram	47
13	SAW interdigitated finger pattern photomask	50
14	Fiber/SAW contact and tuning method	51
15	Experimental amplitude mode coupling efficiency vs. SAW amplitude	52
16	Differential heterodyne phase delay vs. stress for silica sensor element	55
17	Differential heterodyne phase delay vs. stress for polycarbonate sensor element	56
18	Phase discriminator	62
19	Positive-feedback active bandpass filter	63

Abstract

A heterodyne polarimetric sensor with an all-fiber optic frequency shifter is described. A surface acoustic wave couples one fiber optic polarization mode to the other orthogonal mode, with a frequency shift. The interference of these two modes creates a heterodyne signal whose phase is equal to the total path birefringence. By measuring this phase before and after the sensor, common mode phase errors are eliminated.

The SAW device and optical system are analyzed with respect to alignment errors and optical/electronic noise. The effect of this noise on a zero crossing phase discriminator is calculated. Optical phase noise, coherence length limitations, and laser frequency drift are evaluated. Phase noise and frequency drift are reduced to negligible levels by the differential measurement. But the short coherence length of laser diodes will degrade sensor performance for polarization preserving fiber longer than 20 meters, due to the large optical path difference.

Experiments with a SAW device, HeNe laser source, and polarization preserving fiber are described. Heterodyning stress sensors using stress elements of silica and

polycarbonate show good linearity, demonstrating the concept of differential heterodyne measurements with an all-fiber acoustic frequency shifter.

Introduction

Even though fiber optic sensors have matured to commercial applications, many problems still limit their accuracy and utility. Two major problems are optical amplitude and phase noise. To understand the effects of these noise sources we must consider the design of a generic fiber optic sensor as shown in figure 1. An optical source, such as an LED or laser diode, is focused into a fiber optic, which transports light to and from the sensor. Through the sensor, either the amplitude, phase, or polarization state of the light is controlled by the measurand. Pressure, temperature, acceleration, and rotation are some of the measurands which have been demonstrated (1). The receiver usually contains an optical detector with appropriate optical devices to analyze the optical sensor signal.

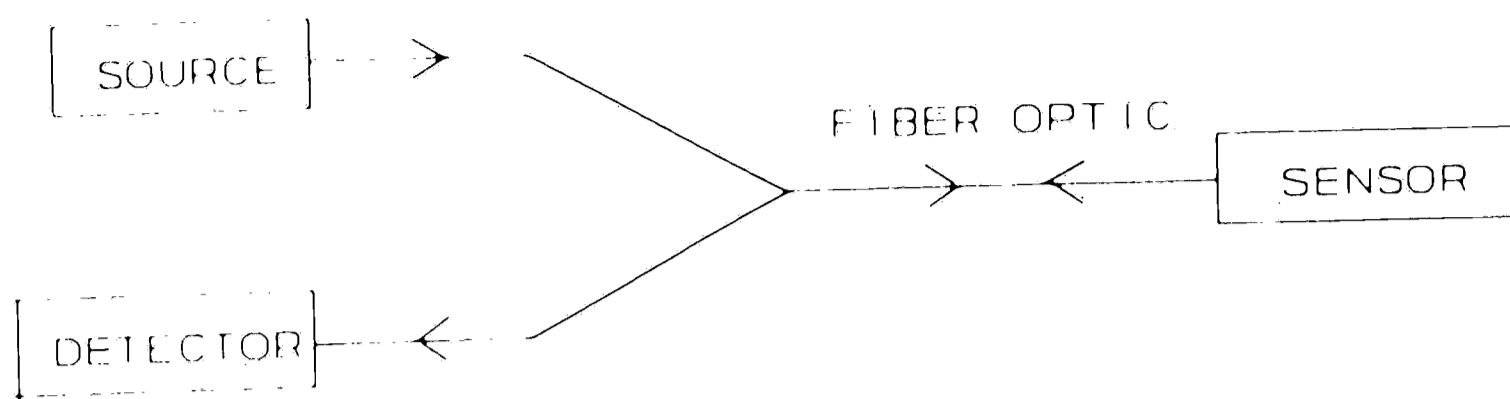


Figure 1. Fiber optic sensor

Intensity sensors, where the measurand controls optical power, are corrupted by amplitude noise of the source and variations of fiber optic attenuation due to thermal and mechanical drift. These noise sources limit the accuracy to approximately 1% (2).

Interferometric sensors, where the measurand controls optical phase, may be affected by both amplitude and phase noise. The optical phase difference between two optical paths, one coupled to the measurand and the other isolated from it, is converted to an amplitude change by optical mixing at either the sensor exit port or the receiver. These two optical paths are combined into a single path in a polarimetric sensor, which senses the phase shift between two polarization modes in a fiber or bulk optic device.

All of these homodyne sensors are sensitive to phase and

attenuation changes in the fiber optic, and to frequency drift and optical phase noise of the source. One method of reducing this noise is to introduce an optical frequency shift on one of the optical paths, heterodyning the sensor phase shift onto a high frequency carrier. This carrier phase is immune to fiber attenuation variations and $1/f$ noise. And errors due to source frequency drift and phase noise are also reduced by measuring the phase before and after the sensor, using differential heterodyne.

This thesis will investigate the performance of a differential heterodyne polarimetric sensor. The sensor consists of a surface acoustic wave optical frequency shifter, polarization preserving fiber optics, birefringent stress sensor, and phase discriminator. Theoretical analysis of the frequency shifter, fiber optics, and sensor will describe the effects of amplitude noise, phase noise, and component misalignment on measurement accuracy. Experiments will demonstrate stress measurement using an elastooptic (or photoelastic) sensor.

Elastooptic Effect

Both the acoustic coupling and sensor birefringence result from the elastooptic effect. Strain in a optical material

creates a deformation of the indicatrix, changing the refractive index for different light polarizations. The indicatrix (see for example Iizuka (3)) describes the refractive index of two orthogonal polarization directions as a function of propagation direction in an anisotropic material. The indicatrix is an ellipsoid of revolution described by equation 1.

$$B_{11}x^2 + B_{22}y^2 + B_{33}z^2 + 2B_{23}yz + 2B_{31}xz + 2B_{12}xy = 1 \quad (1)$$

The B coefficients are related to the strains and elastooptic coefficients by the matrix equation 2.

$$\begin{pmatrix} B_{11} - \frac{1}{n_1^2} \\ B_{22} - \frac{1}{n_2^2} \\ B_{33} - \frac{1}{n_3^2} \\ B_{23} \\ B_{31} \\ B_{12} \end{pmatrix} = \begin{pmatrix} P_{11} & P_{12} & P_{13} & P_{14} & P_{15} & P_{16} \\ P_{21} & P_{22} & P_{23} & P_{24} & P_{25} & P_{26} \\ P_{31} & P_{32} & P_{33} & P_{34} & P_{35} & P_{36} \\ P_{41} & P_{42} & P_{43} & P_{44} & P_{45} & P_{46} \\ P_{51} & P_{52} & P_{53} & P_{54} & P_{55} & P_{56} \\ P_{61} & P_{62} & P_{63} & P_{64} & P_{65} & P_{66} \end{pmatrix} \begin{pmatrix} S_{xx} \\ S_{yy} \\ S_{zz} \\ S_{yz} \\ S_{xz} \\ S_{xy} \end{pmatrix} \quad (2)$$

S_{xx} , S_{yy} , and S_{zz} are principal strains; and S_{yz} , S_{xz} , and S_{xy} are shear strains. n_1 , n_2 , and n_3 are the dimensions of the major axes of the index ellipsoid for zero strain; and P_{ij} are the elastooptic or strain optic coefficients. The stress and stress optic coefficients are related to the strain and

strain optic coefficients, respectively, by Young's modulus of the material. For an isotropic material with coordinate system chosen along the principal axes of the strain tensor, we obtain:

$$S_{xz} = S_{yz} = S_{xy} = 0 \quad (3)$$

Then equation 2 reduces to equation set 4:

$$\begin{aligned} B_{11} - \frac{1}{n_1^2} &= P_{11}S_{xx} + P_{12}[S_{yy} + S_{zz}] \\ B_{22} - \frac{1}{n_2^2} &= P_{11}S_{yy} + P_{12}[S_{xx} + S_{zz}] \\ B_{33} - \frac{1}{n_3^2} &= P_{11}S_{zz} + P_{12}[S_{yy} + S_{xx}] \\ B_{23} &= B_{31} = B_{12} = 0 \end{aligned} \quad (4)$$

And for light propagating along the z direction, the index ellipsoid is described by equation set 5.

$$\begin{aligned} B_{11}x^2 + B_{22}y^2 &= 1 \\ n_1^2 &= \frac{1}{B_{11}} \\ n_2^2 &= \frac{1}{B_{22}} \\ \frac{1}{n_1^2} - \frac{1}{n_2^2} &= (P_{11} - P_{12})(S_{xx} - S_{yy}) \end{aligned} \quad (5)$$

Then the optical phase shift, ϕ , between polarizations in the X and Y directions, over a propagation distance z, is described by equation 6.

$$\phi = 2\pi (n_1 - n_2) \frac{z}{\lambda} = \pi z \frac{n^3}{\lambda} (P_{11} - P_{12}) (S_{xx} - S_{yy}) \quad (6)$$

The optical phase shift, due to strain induced birefringence, is proportional to the propagation distance, the difference between the principal strains, and the difference between the strain optic coefficients. The goal of this thesis is to measure this phase shift by heterodyning the optical phase onto an electronic carrier.

Differential Heterodyne

The birefringent phase shift is interrogated by optical interference of the two polarizations. If these two polarizations are at different optical frequencies, the optical fields are given by

$$\begin{aligned} E_x &= A_x \cos(\omega_x t + \phi_x) \\ E_y &= A_y \cos(\omega_y t + \phi_y) \end{aligned} \quad (7)$$

The interference of these two fields produces an optical intensity proportional to the square of the sum of the fields.

Since the optical detector does not respond to optical

$$\begin{aligned}
I &= (E_x + E_y)^2 \\
&= A_x^2 \cos^2(\omega_x t + \phi_x) + A_y^2 \cos^2(\omega_y t + \phi_y) \\
&\quad + A_x A_y \cos[(\omega_x - \omega_y)t + \phi_x - \phi_y] + A_x A_y \cos[(\omega_x + \omega_y)t + \phi_x + \phi_y]
\end{aligned} \tag{8}$$

frequencies, the detector current is proportional to the time average of the intensity.

$$\begin{aligned}
\langle I(t) \rangle &= \frac{1}{T} \int_0^T I(t) dt \\
&= \frac{1}{2} (A_x^2 + A_y^2) + A_x A_y \cos[(\omega_x - \omega_y)t + \phi_x - \phi_y] \\
\omega_x - \omega_y &\ll \frac{2\pi}{T} \ll \omega_x + \omega_y
\end{aligned} \tag{9}$$

The detector current consists of a constant component and the heterodyne interference term, at the difference frequency, which carries the optical phase information. This difference frequency may be chosen in the Mhz region to avoid 1/f system noise and allow measurement of high bandwidth measurands.

The differential heterodyne measurement is illustrated in figure 2. The source excites one mode in a 2 mode fiber optic. These modes are either polarization eigenmodes or spatial modes of the fiber. Figure 2 shows these modes as two electric field components, E_x and E_y . A frequency shifting device transfers power between the modes with an accompanying frequency shift. For the case of polarization modes, the two modes propagate down polarization preserving

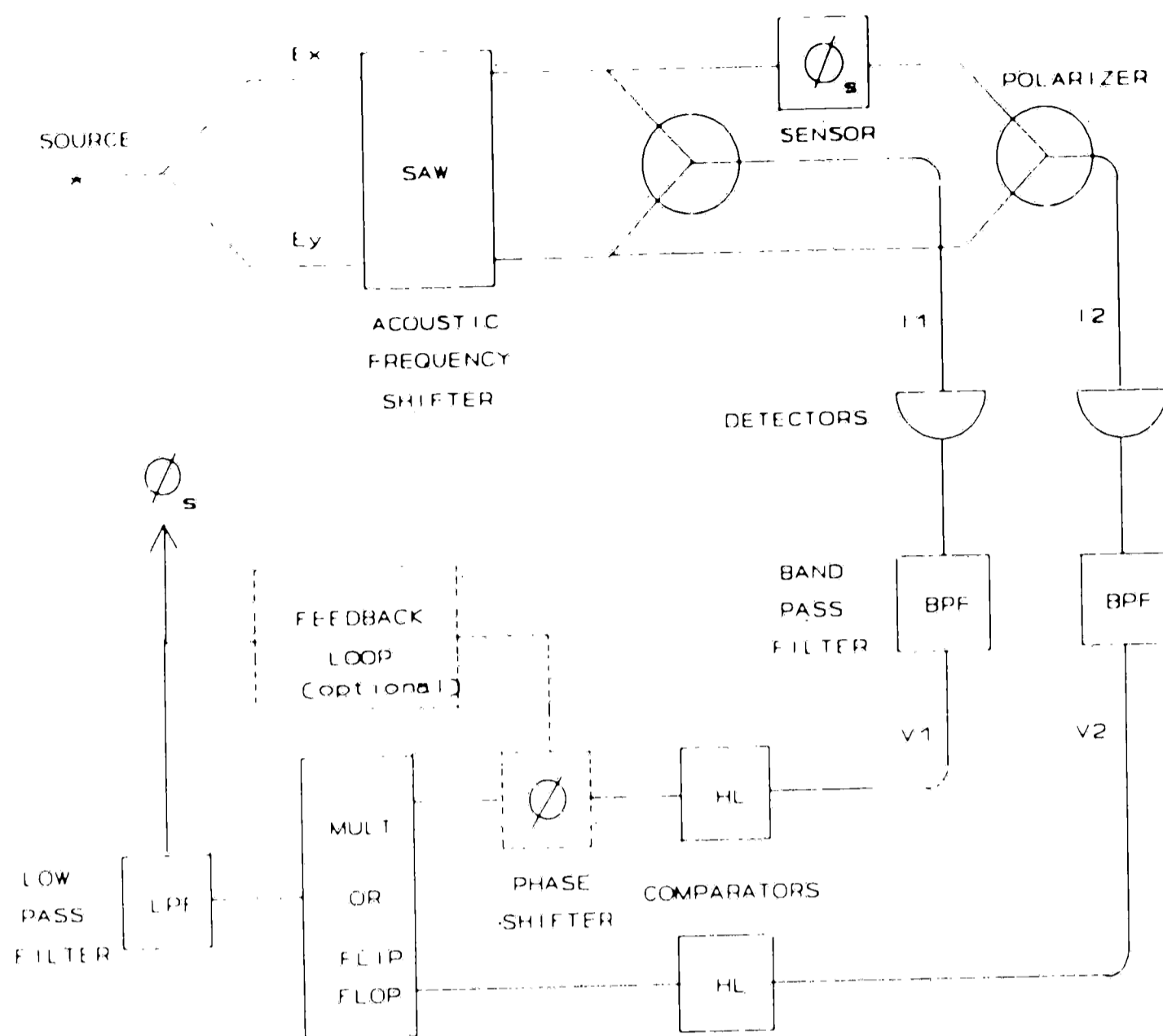


Figure 2. Differential heterodyne polarimetric sensor system

fiber optic to the sensor. The sensor may be an optical element, a planar waveguide, or optical fiber. In each case the measurand creates birefringence in the sensor, which must be measured in the presence of birefringence drift of the fiber and amplitude/phase noise in the laser source. To reduce these error sources, the heterodyne phase is measured directly before and after the sensor; the phase difference is then primarily due to the birefringent phase shift of the

sensor. For a polarimetric measurement, these two heterodyne signals are produced by polarizers with axes at 45 degrees to the eigenmodes of the fiber. Each polarizer coherently combines the eigenmodes to produce an interference function, as described previously in equation 8. Intensities 1 and 2 are outputs of polarizers before and after the sensor, respectively.

$$\begin{aligned} \langle I_1(t) \rangle &= \frac{1}{2} (A_{1x}^2 + A_{1y}^2) + A_{1x}A_{1y} \cos[(\omega_{1x} - \omega_{1y})t + \phi_{1x} - \phi_{1y}] \\ \langle I_2(t) \rangle &= \frac{1}{2} (A_{2x}^2 + A_{2y}^2) + A_{2x}A_{2y} \cos[(\omega_{2x} - \omega_{2y})t + \phi_{2x} - \phi_{2y}] \end{aligned} \quad (10)$$

These interference signals are transferred to detectors via two multimode fiber optics. The detector currents pass through electrical bandpass filters which are centered on the heterodyne frequency, with sufficient bandwidth to accommodate the measurand. The differential phase of these filtered signals is equal to the birefringence of the sensor. Since laser phase noise and stress induced birefringence drift, in the polarization preserving fiber optics, are present in intensities 1 and 2, they are rejected as common mode in the differential measurement.

$$\phi_s = (\phi_{2x} - \phi_{2y}) - (\phi_{1x} - \phi_{1y}) \quad (11)$$

The differential phase is measured by a phase discriminator consisting of two comparators, a flip-flop or multiplier,

and a low pass filter with bandpass equal to the bandwidth of the measurand. Details of this discriminator are found in appendix A.

The complete fiber optic sensor system is configured with the laser source, frequency shifter, detectors, filters, and discriminator in one electronic module. This module connects to the sensor and polarizers through one polarization preserving (high birefringence single mode) fiber optic and two multimode fibers.

Frequency Shifting Devices

The many needs for optical frequency shifting has created many different approaches. Coherent communications (4), heterodyning gyros (5,6), Doppler velocimeters (7), heterodyne interferometers (8,9), and frequency domain reflectometers (10,11) all require small shifts of optical carrier frequency. Most frequency shifters belong to one of three types: direct laser modulation, serrodyne, or refractive index perturbing. Typically refractive index types employ the Doppler shift from a travelling refractive index wave. Serrodyne techniques involve a linear time ramp of optical phase.

Conventional Bragg cells are most common of the refractive index types. A travelling index wave is created, through the elastooptic effect, by a bulk acoustic wave in an optical material. This index wave acts as a travelling Bragg diffraction grating, producing diffracted orders which are Doppler shifted from the zero order (undiffracted light). See Yariv (12) for a detailed theoretical description. This technology is commercially available and capable of high diffraction efficiency. However, interfacing optics are required for coupling to fiber optics.

The easiest method is direct current modulation of a laser diode (13, 14 , 15). Diode temperature and carrier density change with diode current. The carrier density changes the cavity refractive index and ohmic heating changes both the refractive index and laser cavity length, shifting the cavity resonant frequency. Thermal effects account for a shift of approximately 7 GHz/mA. However, due to thermal inertia of the laser chip, the total shift reduces to only the carrier induced component (0.1 GHz/mA) at modulation frequencies above 10 Mhz. This technique shows promise for non-polarimetric differential heterodyne interferometers using ramped frequency scanning and fringe counting; and it should be considered for future work.

The serrodyne method consists of an electrooptic phase

shifter, in either bulk optic or waveguide configuration. The electrode voltage is ramped with a sawtooth function, creating a ramped phase function with a constant frequency shift. Due to the large voltage slew rate required, the ramp must be broken into a sawtooth function. This method has two deficiencies, discontinuities in the frequency shift and optical interfacing required to separate the two polarizations, shift one of them, and recombine into a single fiber. Also the flyback of the sawtooth and nonlinearities of the ramp create unwanted frequency components.

The need for interfacing optics is eliminated by generating the frequency shifted component in the fiber.

Acoustic perturbation of polarization preserving fiber optic creates frequency shifting by coupling polarization modes of the fiber. For example, Nosu et al (17) used cylindrical PZT resonators, spaced by the $3/4$ of a beat length of the fiber. By driving alternate resonators 90 degrees out of phase, a frequency shifted component will be coupled between polarization modes. 3% conversion efficiency was demonstrated at 4.675 Mhz.

Another in-fiber method capable of higher conversion efficiency was demonstrated by Risk et al (18,19,20,21). Polarization preserving fiber is pressed against a surface

acoustic wave to acoustically couple one mode to the other with a Doppler frequency shift. This method was first demonstrated with an edge PZT transducer on a silica substrate. To obtain sufficient coupling efficiency, this small edge transducer was driven in pulsed mode at 32 watts peak, with 26% conversion efficiency. Continuous operation would overheat the device. A later version was demonstrated by Greenhalgh, et al, (22) using an interdigitated finger pattern on a piezoelectric substrate. 4.1 % conversion efficiency was demonstrated with 1.9 watts continuous. This surface acoustic wave (SAW) device was chosen as the most promising candidate for the demonstration of a differential heterodyne sensor.

Surface Acoustic Wave Frequency Shifter

The SAW frequency shifter is based upon acoustically induced mode coupling in polarization preserving fiber optic. Mode coupling due to periodic stress was first demonstrated by Youngquist et al (23). Polarization preserving fiber optic, sometimes called HiBi fiber, exhibits very small coupling of polarization eigenmodes during propagation along the fiber. This is accomplished by creating a very high birefringence in the fiber core, through core shape asymmetry or stress. The beat length of the fiber is the distance over which the

birefringent phase shift equals 2π . It is related to the fiber core birefringence Δn by:

$$L_B = \frac{\lambda_0}{\Delta n} \quad (12)$$

Only environmental perturbations, such as external pressure or bending, with spatial wavelengths near the beat length will couple these eigenmodes of the fiber. So typical fibers, with beat lengths below 2 mm, are very resistant to polarization mode coupling from environmental stresses.

Additional birefringence Δn_p may be created by pressing the fiber between two flat plates.

$$\Delta n_p = \frac{0.79 n^3 C_o S_p}{d} \quad (13)$$

Where S_p is the force per unit length of fiber, C_o is the differential stress optic coefficient (see equation 68), d is the fiber diameter, and n is the core refractive index. For silica core fiber optic, $C_o = 5 \times 10^{-13} \text{ cm}^2/\text{dyne}$ and $n = 1.46$. If this stress is at 45 degrees with respect to the principal fiber axes, the principal polarization axes of the fiber are rotated by an angle θ_r (see Youngquist et al (23)) given by equation 14.

If the fiber is periodically compressed, a fraction $\sin^2(2\theta_r)$

$$\text{SIN}(\theta_r) = \left(\frac{\Delta n_p^2}{2(\Delta n_p^2 + \Delta n^2 + \sqrt{2}\Delta n\Delta n_p)} \right)^{1/2} \quad (14)$$

of polarization power in one axis will be coupled to the other polarization after each compression. By spacing these compressions at intervals of the beat length, the coupling will accumulate due to phase matching of the polarizations at the compression points. One might expect to see a Doppler optical frequency shift in the coupled polarization if the periodic stress field moves along the fiber at a constant velocity. A surface acoustic wave creates a periodic stress field, moving at the acoustic velocity of the SAW substrate. The frequency shift and coupling efficiency of this interaction are easily evaluated through the coupled mode equations.

The coupled mode equations (Yariv (24)) describe the evolution of E fields of two coupled modes. The modes may be spatial or polarization modes. In the case of polarization modes, the coupling of the x and y polarization axes is dependent upon the propagation constants, β_x and β_y , and the coupling coefficient $a(z)$. Assuming that the stress creates negligible change in the propagation constants, the coupled mode equations are described by equation set 15.

$$\begin{aligned}\frac{dE_x}{dz} &= a(z) E_y e^{-i(\beta_x - \beta_y)z} \\ \frac{dE_y}{dz} &= -a(z) E_x e^{+i(\beta_x - \beta_y)z}\end{aligned}\tag{15}$$

As shown by equations 13 and 14, the E field coupling coefficient is proportional to θ_r , Δn_p , and S_p , for small Δn_p . So the E field coupling coefficient is proportional to the stress, which is proportional to the amplitude of the surface acoustic wave, as shown in equation 16.

$$\begin{aligned}a(z) &= A e^{-i(\omega_a t - k_a z)} \\ A &= K_f A_0\end{aligned}\tag{16}$$

A_0 , ω_a , and k_a are the amplitude, angular frequency and propagation constant, respectively, of the surface acoustic wave. And K_f is the fiber/acoustic coupling constant which depends upon contact pressure, fiber design, and fiber orientation. The analogy between equation 15 and Yariv's generalized form for the coupled mode equations, allows use of his solution for these coupled differential equations. For the case where all of the optical power is in the y polarization mode at $z=0$, the optical electric field for the x polarization as a function of distance along the fiber, z , is

$$E_x(z) = E_y(0) \frac{2Ai}{(4A^2 + (\Delta k)^2)^{1/2}} \sin\left[\frac{1}{2}(4A^2 + (\Delta k)^2)^{1/2}z\right] e^{-i\beta_x z} \quad (17)$$

and the corresponding y polarization is described by

$$E_y(z) = E_y(0) \left\{ \cos\left[\frac{1}{2}(4A^2 + (\Delta k)^2)^{1/2}z\right] - i \frac{\Delta k}{(4A^2 + (\Delta k)^2)^{1/2}} \sin\left[\frac{1}{2}(4A^2 + (\Delta k)^2)^{1/2}z\right] \right\} e^{-i\beta_y z} \quad (18)$$

The optical power coupling efficiency from the y polarization to the x polarization is

$$\eta = \frac{E_x^2(z)}{E_y^2(0)} = \frac{4A^2}{4A^2 + (\Delta k)^2} \sin^2\left(\frac{1}{2}(4A^2 + (\Delta k)^2)^{1/2}z\right) \quad (19)$$

Where Δk is the phase mismatch between the fiber birefringence and the propagation constant of the acoustic wave.

$$\Delta k = \beta_x - \beta_y - k_a \quad (20)$$

The power coupling efficiency is maximized at the phase match condition $\Delta k = 0$. Conservation of energy allows two solutions for the accompanying frequency shift, whose sign

depends on the propagation direction of the surface acoustic wave. Assuming the y polarization to be the fast axis of the fiber, the following equations hold.

$$\begin{array}{ll}
 \text{copropagating} & k_a = \beta_x - \beta_y \\
 \text{counter-propagating} & k_a = \beta_y - \beta_x
 \end{array}
 \quad
 \begin{array}{l}
 \omega_a = \omega_x - \omega_y \\
 \omega_a = \omega_y - \omega_x
 \end{array}
 \quad (21)$$

The sign of the frequency shift is determined by the direction of the coupling, from fast to slow axis, or the direction of the SAW wave relative to the optical propagation direction. In this work the direction of the frequency shift is not important, because shifts in either direction will produce identical heterodyne signals.

Figure 3 shows the x and y polarization power vs. a propagation distance parameter Az/π , for the case where $\Delta k = 2A$. Without phase matching, 100% coupling never occurs. Only part of the total optical power is transferred back and forth between the two polarization modes as they propagate down the fiber. The effect of phase mismatch is most easily understood by converting equation 19 into equation 22.

$$\eta = \gamma^2 \text{SIN}^2 \left(\frac{AZ}{\gamma} \right)$$

$$\gamma = \left(\frac{1}{1 + \left(\frac{\Delta k}{2A} \right)^2} \right)^{1/2} \quad (22)$$

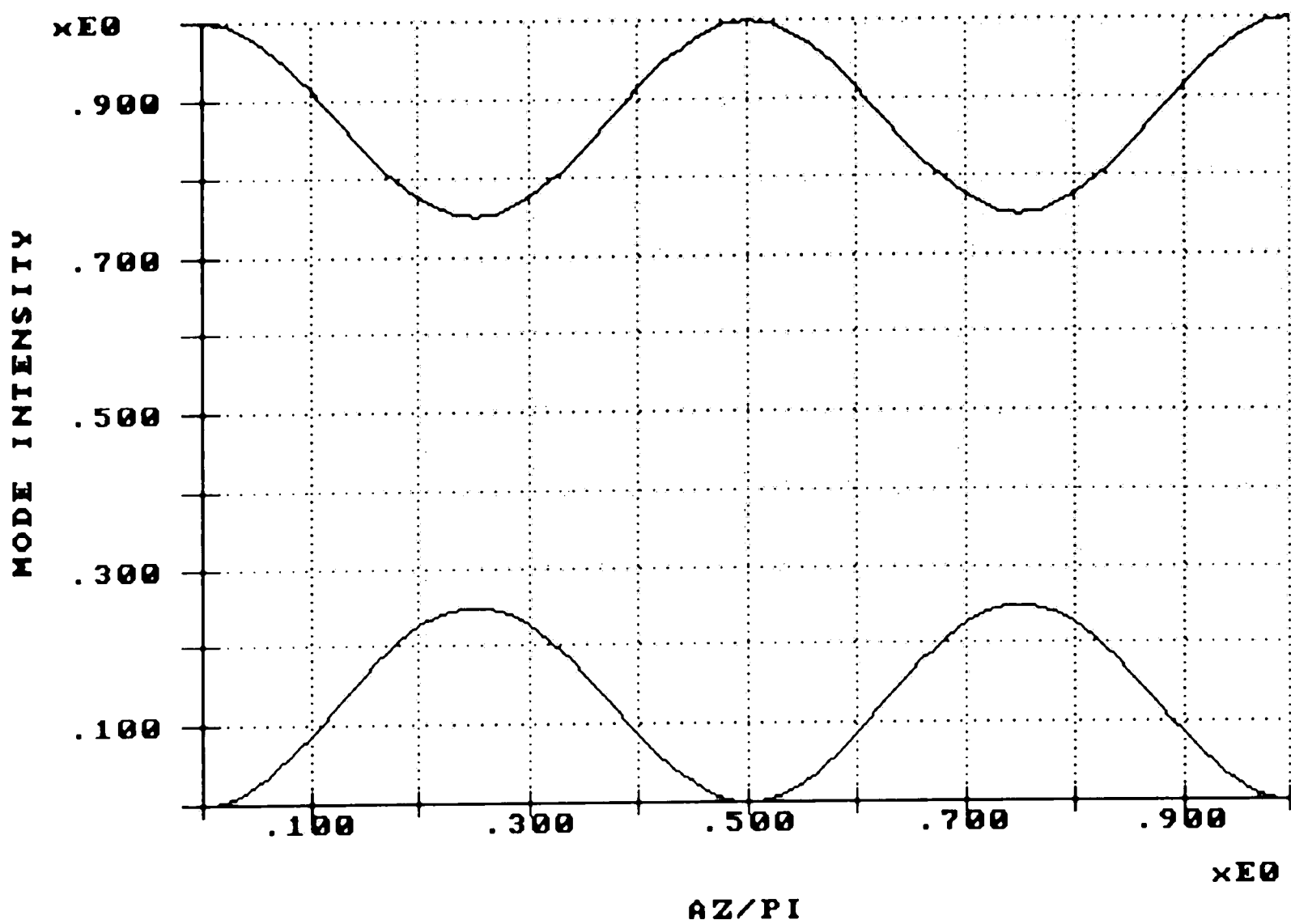


Figure 3. Polarization intensities I_x (lower) and I_y (upper) vs. distance parameter Az/π for $\Delta k=2A$

The peak power coupling efficiency is reduced to γ^2 and peak coupling points occur at $z = (N + 1/2)\gamma\pi/A$, where N is an integer ($N = 0, 1, 2, \dots$).

The Δk dependence is better demonstrated by another form of equation 19.

$$\eta = A^2 z^2 \text{SINC}^2 \left[\frac{1}{2} (4A^2 + (\Delta k)^2)^{1/2} z \right] \quad (23)$$

where $\text{SINC}(X) = \text{SIN}(X)/X$. The zeros of the coupling efficiency occur at

$$\Delta k_m = \left(\left(\frac{2m\pi}{z} \right)^2 - 4A^2 \right)^{1/2} \quad (24)$$

where m is an integer. The phase matching condition places constraints on the acoustic wave geometry and frequency as shown in the next section on SAW devices.

Surface Acoustic Waves

The surface acoustic wave, or Rayleigh wave, consists of surface wave motions, in the y and z directions, which are 90 degrees out of phase. Here z is the propagation direction and y is perpendicular to the substrate surface. The displacement of the solid only occurs within a few acoustic wavelengths of the surface. Surface acoustic waves are generated by either edge or interdigitated transducer (IDT). Due to its superior bulk wave suppression and higher efficiency, only the IDT will be considered in this work.

Figure 4 shows the IDT surface acoustic wave device with both transmitting and receiving transducers. The transmitting IDT produces a surface acoustic wave with

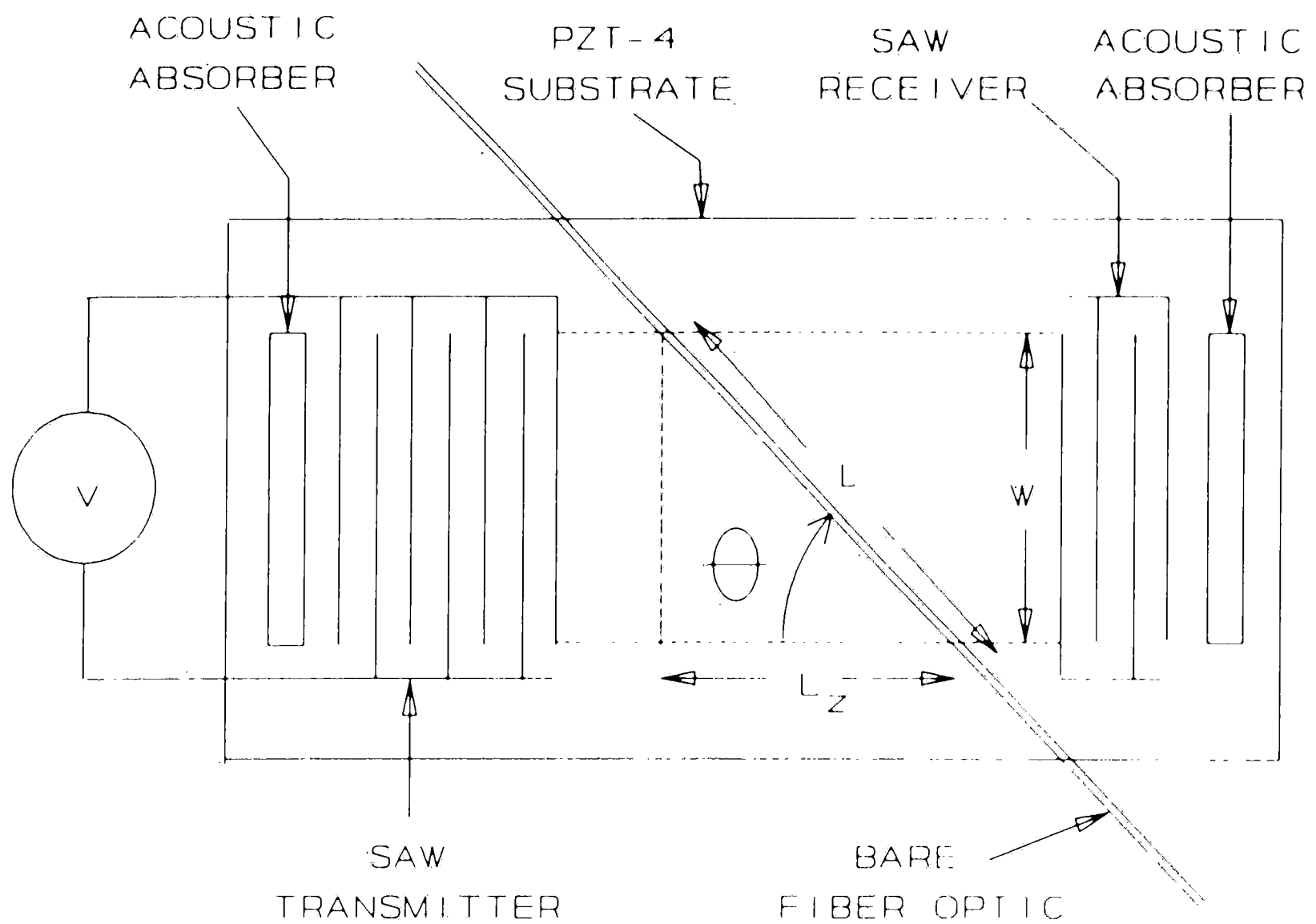


Figure 4. Diagram of surface acoustic wave device and fiber optic

acoustic aperture W , surface amplitude A in the y direction, acoustic wavelength λ_a , acoustic frequency f , and velocity v_a . To provide phase matching, the polarization preserving fiber optic contacts the surface at an angle θ with respect to the propagation direction z . For this configuration the phase matching condition is described by equation 25.

$$\Delta k = 2\pi \left(\frac{1}{L_B} - \frac{f \cos\theta}{v_a} \right) \quad (25)$$

The acoustic frequency of the IDT is limited to a small range by a resonant effect which is determined by the interdigitated finger number and spacing (see equation 30). So fibers with various beat lengths are phase matched by adjusting θ . Equation 23 may be rewritten in terms of the acoustic wave/fiber interaction length L and α which is the ratio of A to the value of A required for 100% coupling with $\Delta k = 0$.

$$\eta = \frac{\alpha^2 \pi^2}{4} \text{SINC}^2 \left(\frac{\alpha \pi}{2} \left[1 - \left(\frac{\Delta k L}{\pi \alpha} \right) \right]^{1/2} \right) \quad (26)$$

Figure 5 shows the coupling efficiency vs. θ for $\alpha = 1$, at the optimum acoustic frequency. Other parameters assumed are beat length of 1.61 mm and a surface acoustic velocity of 2111 M/s for a PZT-4 piezoelectric substrate.

The half power angular range of 2.5 degrees (FWHM) indicates the need for accurate angular alignment. The frequency dependence at optimum θ (figure 6) shows a half power bandwidth of 94 Khz (FWHM).

A complete analysis of mode coupling efficiency must include

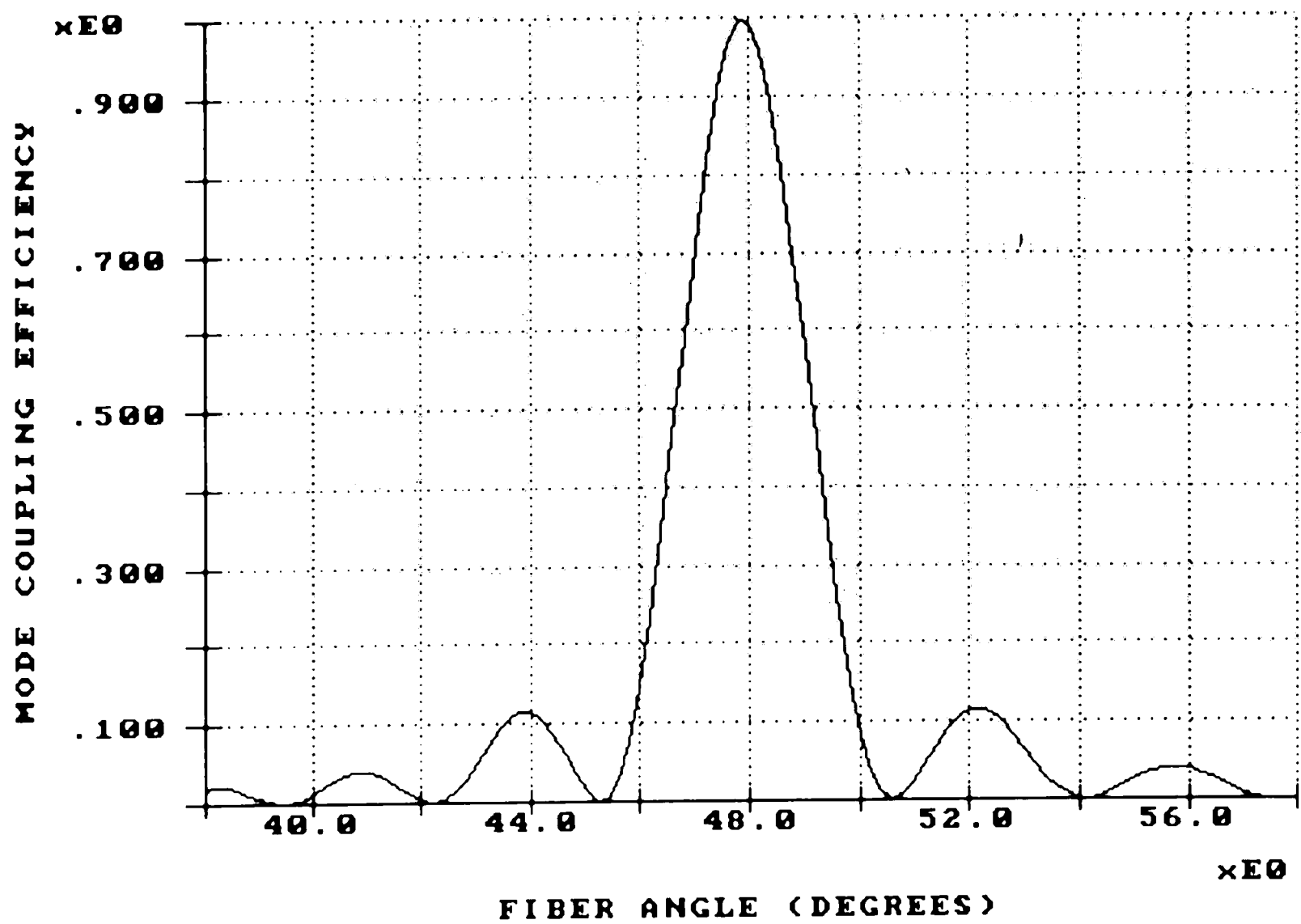


Figure 5. Mode coupling efficiency vs. fiber angle θ

the frequency dependence of A_0 , the SAW amplitude. The electrical to acoustic frequency response of the SAW device is determined by the periodicity of the IDT structure. One of the simplest models of an IDT is the delta function model (see Datta (25), Campbell (26), and Matthews (27)) which approximates the actual voltage distribution on the piezoelectric substrate by a set of delta functions as shown in figure 7.

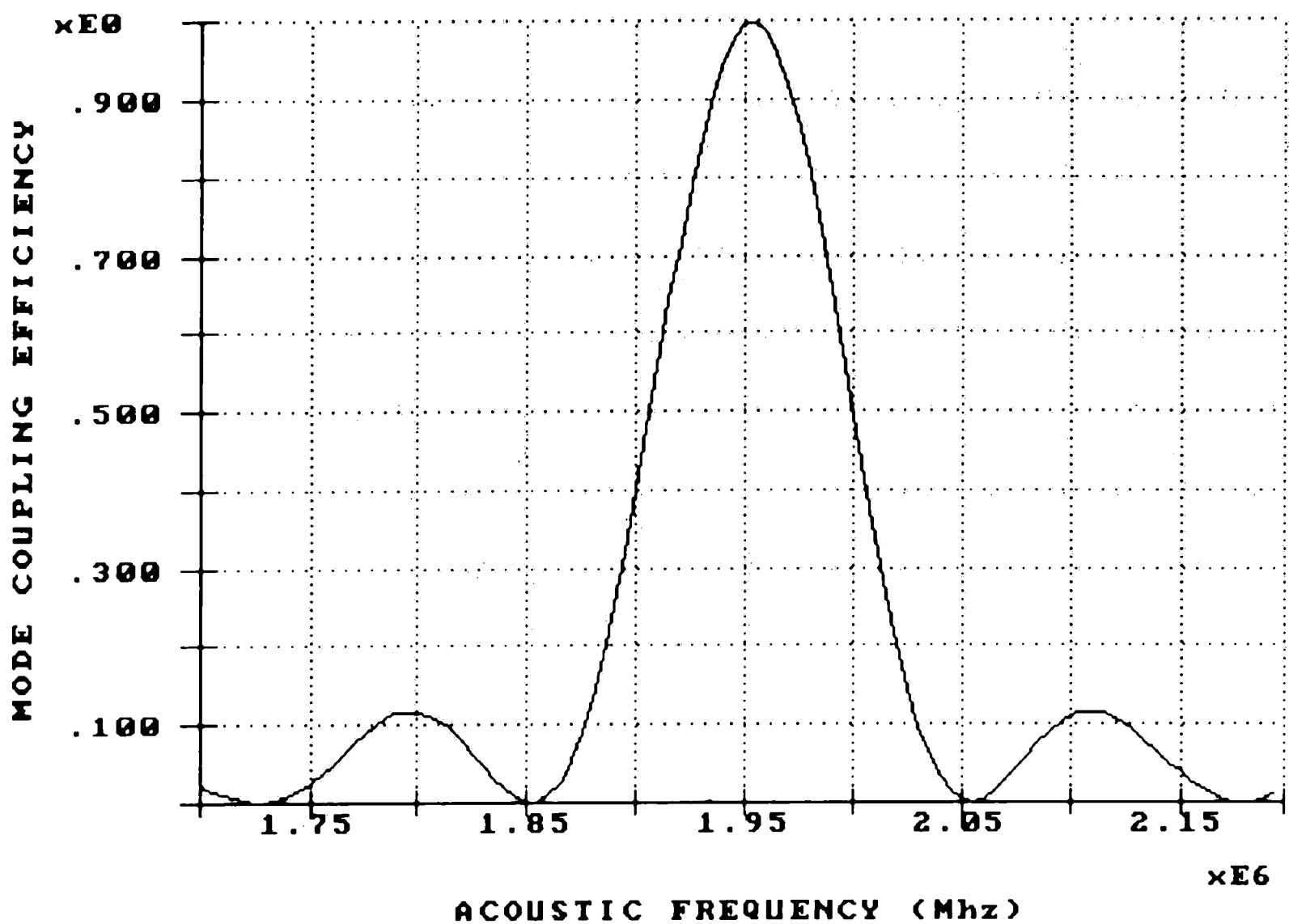


Figure 6. Mode coupling efficiency vs. acoustic frequency at optimum fiber angle θ

The amplitude A_0 of the acoustic wave is

$$A_0 = C_y u V \quad (27)$$

where V is the voltage across the IDT, C_y is the ratio of surface displacement to electrode voltage, and u is the response function describing the array of voltage delta functions, which represent the array of interdigitated fingers.

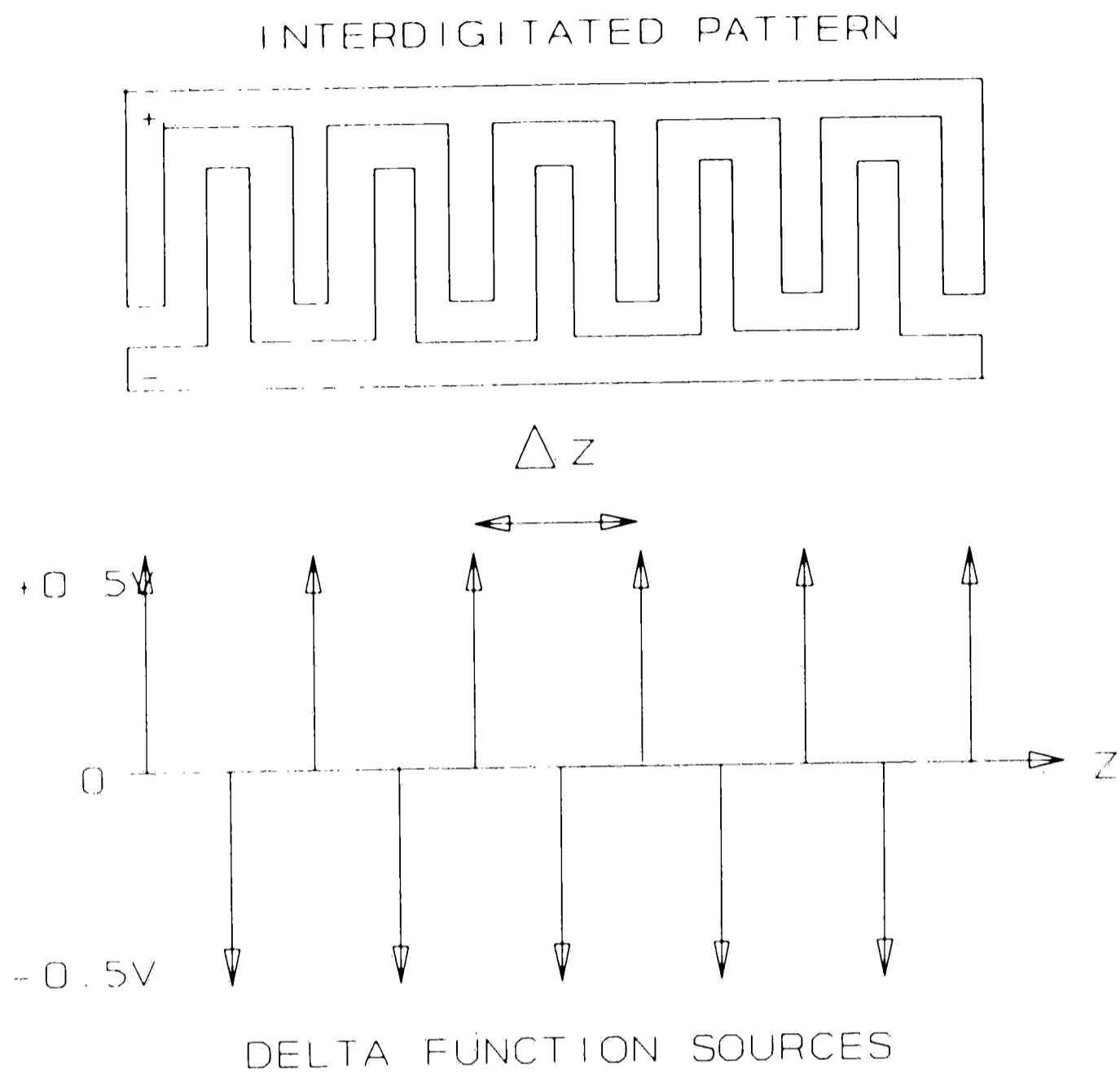


Figure 7. Delta function model for an interdigitated SAW device

$$u = 0.8i K^2 \sum_{n=1}^N \frac{1}{2} (-1)^n e^{-ik_a z_n} \quad (28)$$

u is imaginary because the amplitude of the wave in the y direction is 90 degrees out of phase with the z direction.

The 0.8 factor corrects for the finger width, which equals the interfinger spacing in this case; and K is the piezoelectric coupling constant. The factor before the exponential describes the finger voltages which alternate between $+V/2$ and $-V/2$. Replacing k_x by $2\pi f/v_x$ and defining the resonant frequency $f_0 = v_x/\Delta z$, $u(f)$ becomes

$$u = 0.8i K^2 N_p \text{SINC}[N_p \pi (f - f_0) / f_0] \quad (29)$$

where N_p is the number of positive fingers. Combining equations 27 and 29, we obtain the acoustic wave amplitude.

$$A_0 = 0.8i K^2 K_f C_y V N_p \text{SINC}[N_p \pi (f - f_0) / f_0] \quad (30)$$

The SAW amplitude is proportional to the number of fingers. But the SAW transducer bandwidth is proportional to $1/N_p$.

The total coupling efficiency, η , includes the effects of electronic to acoustic and acoustic to fiber mode phase matching. These two effects are combined in equation 26 by redefining α to include the frequency dependence of the acoustic amplitude A_0 .

$$\alpha = \frac{V}{V_m} \text{SINC}[N_p \pi (f - f_0) / f_0] \quad (31)$$

Where V_m is the transducer voltage required for 100% mode

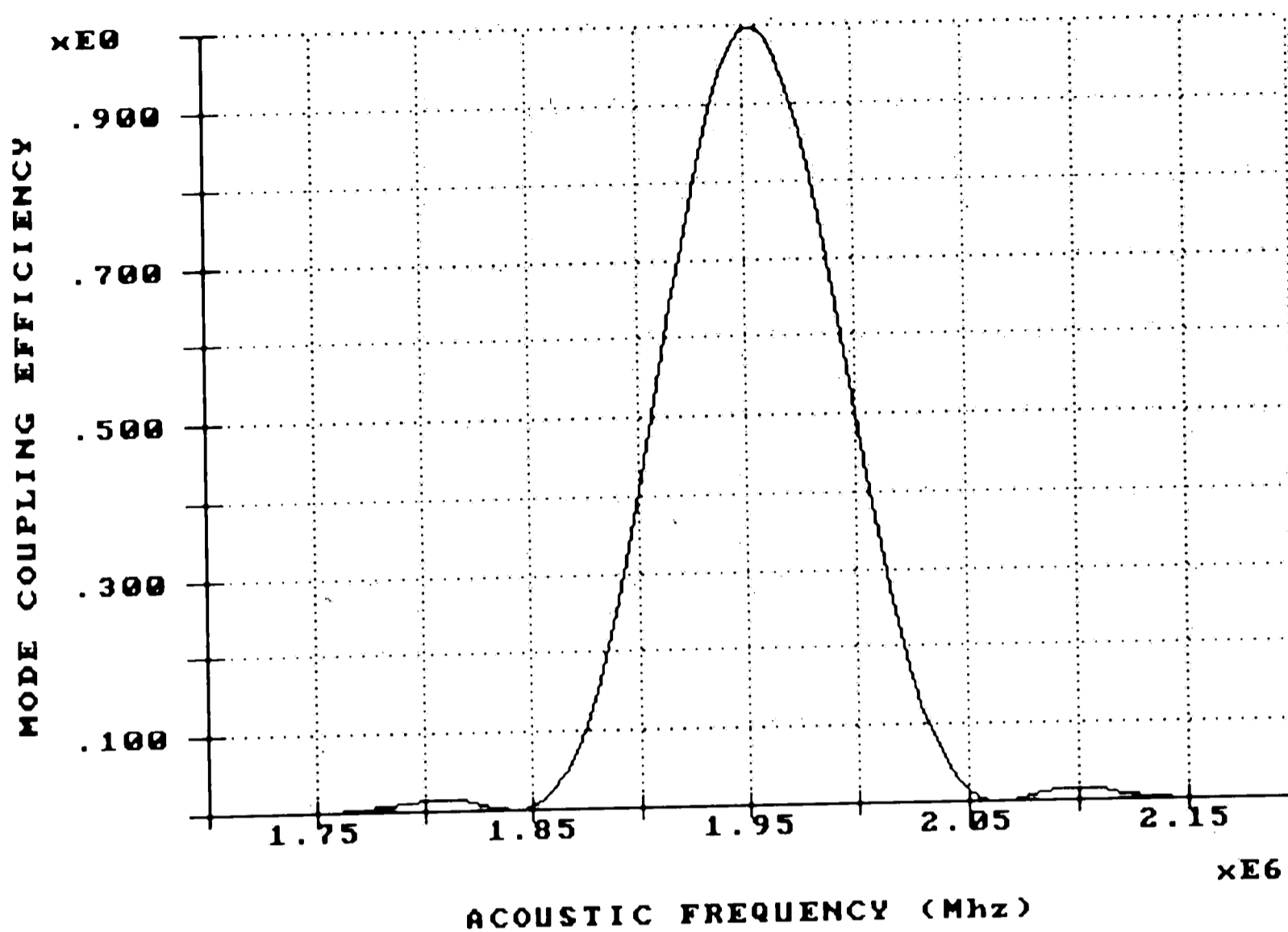


Figure 8. Mode coupling efficiency vs. acoustic frequency, including SAW frequency response at $\Delta k=0$

coupling with phase matching ($\Delta k = 0$). The experimental case considered here uses an IDT with 19 fingers ($N_p = (N-1)/2 = 9$) and an acoustic wavelength of 1.08 mm. The SAW transducer bandwidth is 200 KHz. The coupling efficiency vs. SAW frequency is shown in figure 8 for this case when $V = V_m$. Notice (comparing figures 6 and 8) that the effect of electronic to acoustic phase matching only causes reduction of the secondary lobes, because the bandwidth of the SAW is approximately twice that of the fiber/acoustic coupling.

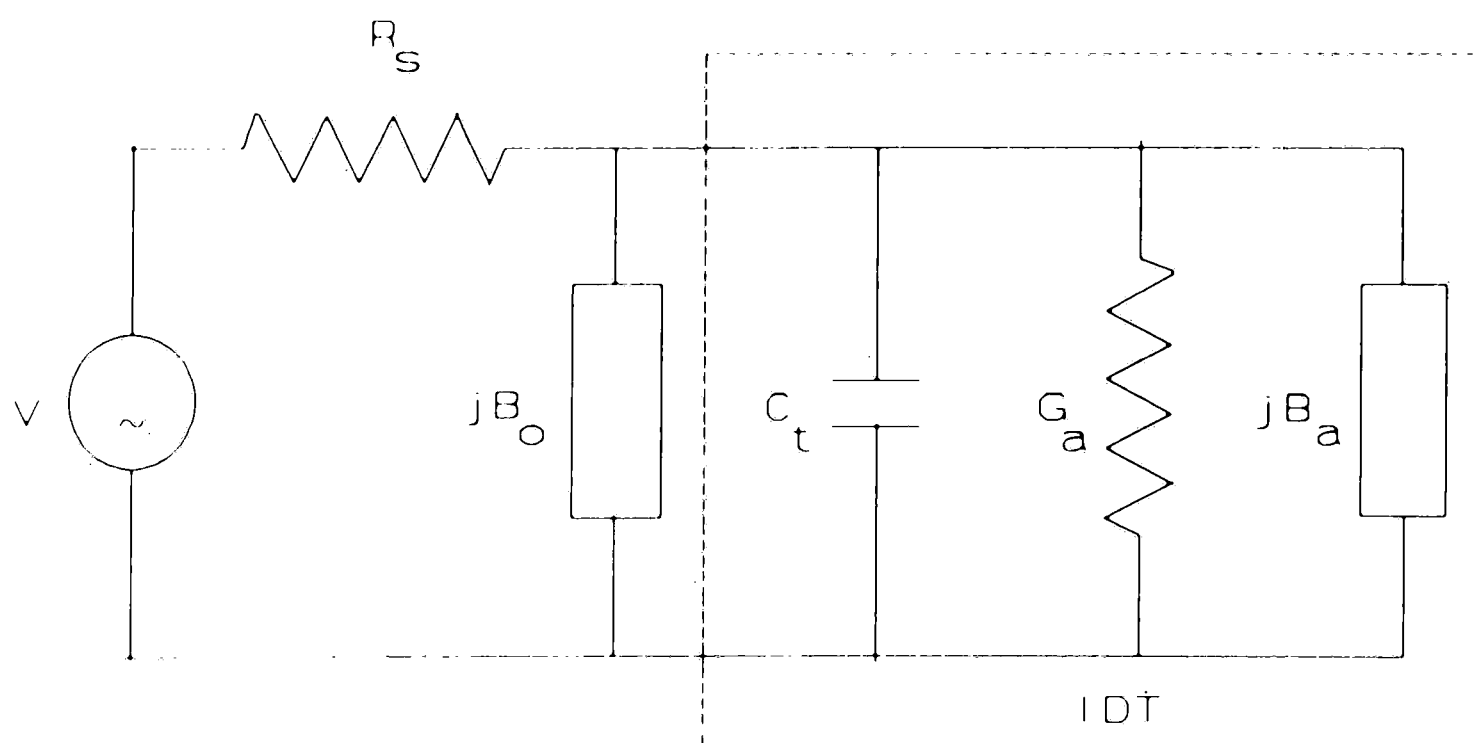


Figure 9. Equivalent circuit for the interdigitated SAW device

Evaluation of the IDT in terms of acoustic power, instead of voltage, offers better insight into the optimal dimensions for the SAW device. Figure 9 shows the equivalent circuit for the electrical voltage source V and the IDT.

The IDT is essentially a capacitor C_t plus an acoustic admittance $G_a(f) + iB_a(f)$ where $G_a(f)$ is the radiation conductance and $B_a(f)$ is the radiation susceptance, which is the Hilbert transform of G_a (see Datta (25)). Power transfer, from the source to the SAW device, is optimized by use of an impedance matching reactance B_o .

$$B_0(f) = -B_a(f) - \omega_a C_t \quad (32)$$

Since $1/G_a$ is usually much greater than the source impedance R_s (50Ω), the electrical power coupled into the acoustic wave is

$$P = \frac{1}{2} |V|^2 G_a \quad (33)$$

where G_a is a function of the piezoelectric coupling constant K , the equivalent dielectric constant C_y , and W the acoustic aperture of the acoustic wave (see reference 25).

$$G_a = \frac{4\pi C_y V_a |u|^2 W}{K^2 \lambda_a} \quad (34)$$

Then combining equations 27 and 34, the acoustic wave amplitude A_0 is related to the power and acoustic aperture.

$$A_0^2 = \frac{C_y^2 K^2 \lambda_a P}{2\pi C_y V_a W} \quad (35)$$

And for the phase matched case, $\Delta k = 0$ and $AL < 0.1$ the coupling efficiency is approximately

$$\eta = A^2 L^2 = A_0^2 K_f^2 L^2 \quad (36)$$

Defining L in terms of the fiber interaction length L_z along the z direction (see figure 4)

$$L^2 = L_z^2 + W^2 \quad (37)$$

the coupling efficiency becomes

$$\eta = \frac{PC_y^2 K^2 K_f^2 \lambda_a (L_z^2 + W^2)}{2\pi C_B V_a W} \quad (38)$$

As indicated by equation 38, power efficiency is maximized by choosing a substrate material with a large piezoelectric coupling constant K . PZT-4 (lead zirconate-titanate) has a very high K , $K = 71\%$ (reference 28). The coupling efficiency also increases as the square of the interaction length L_z ; but due to acoustic diffraction, the acoustic amplitude diminishes beyond lengths $L_z > W^2/\lambda_a$. The coupling efficiency also increases as the acoustic aperture W and θ approach zero. So the fiber/acoustic interaction region should be long and narrow, but within the constraints of acoustic diffraction and localized power dissipation in the substrate. A wider acoustic aperture was utilized in this work to accommodate a wide range of fiber optic beat lengths and fiber angles, while still maintaining moderate efficiency over the entire range.

Polarization Analysis

Figure 10 shows polarization states at different points in

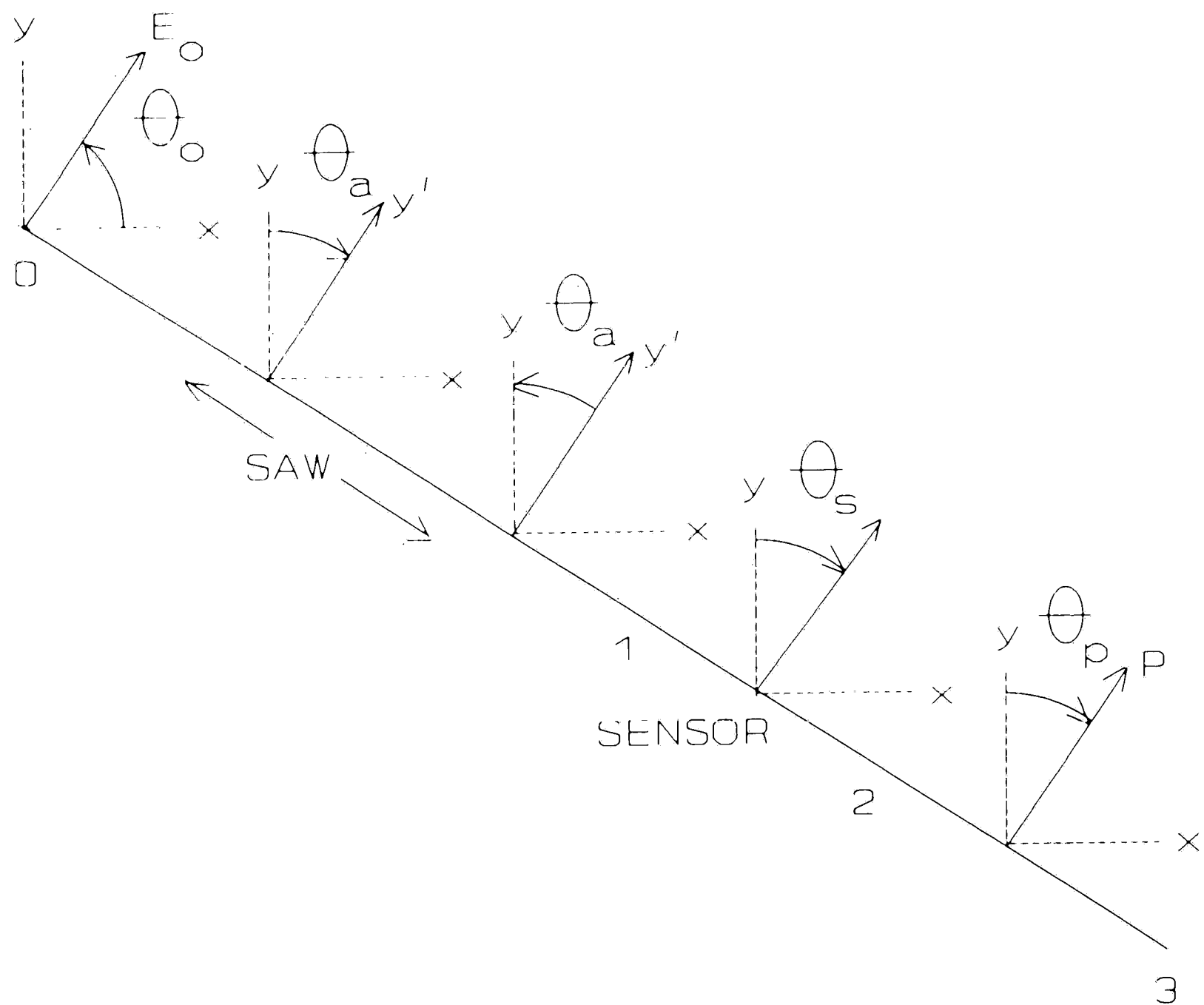


Figure 10. Polarization axis orientations at various points in the optical system

the sensor system. The x and y axes are the principal polarization axes of the unstressed polarization preserving fiber optic. Ideally, the polarization at the fiber entrance

and the sensor principal stress axes are parallel to either x or y; θ_0 and θ_1 are the errors in these alignments, respectively. θ_p is the angle of the final polarizer.

The electric field vector transfer function of the fiber/SAW interaction consists of three Jones matrices: two polarization rotations and mode coupling. Once the fiber/SAW angle θ is aligned mechanically, any residual phase mismatch is eliminated by fine tuning the acoustic frequency within the bandwidth of the IDT. So typically phase matching is easily obtained. Assuming $\Delta k = 0$, equations 17 and 18 become

$$\begin{aligned} E_x(z) &= iE_y(0) \sin(Az) e^{-i\beta_x z} \rightarrow iE_y(0) \sqrt{\eta} e^{-i\phi_a} \\ E_y(z) &= E_y(0) \cos(Az) e^{-i\beta_y z} \rightarrow E_y(0) \sqrt{\eta-1} \\ \phi_a &= (\beta_x - \beta_y) z \end{aligned} \quad (39)$$

where ϕ_a is the fiber birefringent phase shift in the region of the SAW/fiber interaction. The Jones matrix form of equation 39 is (also see Rashleigh (29) and Risk (30))

$$M(\eta, \phi, \omega) = \begin{vmatrix} \sqrt{1-\eta} e^{-i\phi} & i\sqrt{\eta} e^{i(\omega t - \phi)} \\ i\sqrt{\eta} e^{-i\omega t} & \sqrt{1-\eta} \end{vmatrix} \quad (40)$$

Contact between the fiber and SAW is maintained by a compressive force which causes rotation of the fiber

principal axes as described by equation 14. The axes rotate by an angle θ_1 in the compressed region and rotate back to the unstressed axes after the SAW interaction. The Jones matrix for axes rotation is

$$R(\theta) = \begin{vmatrix} \cos(\theta) & \sin(\theta) \\ -\sin(\theta) & \cos(\theta) \end{vmatrix} \quad (41)$$

Further coupling between the fiber polarization modes occurs in the portion of the fiber between the SAW and the sensor. Mechanical perturbations whose spatial frequencies match the fiber beat length will couple these modes. Essentially this interaction is described by the Jones matrix $M(\eta_f, \phi_f, 0)$, where subscript f designates values for the statically stressed fiber, with no frequency shift. So the total fiber/SAW interaction and fiber link to the sensor is described by the Jones matrix equation (see figure 10)

$$\vec{E}_1 = M(\eta_f, \phi_f, 0) R(-\theta_a) M(\eta_a, \phi_a, \omega_a) R(\theta_a) \vec{E}_0 \quad (42)$$

where

$$\vec{E}_i = \begin{vmatrix} E_{ix} \\ E_{iy} \end{vmatrix} \quad (43)$$

$$\vec{E}_0 = \begin{vmatrix} \cos(\theta_0) \\ \sin(\theta_0) \end{vmatrix} |E_0|$$

Assuming small θ_0 and θ_a , and neglecting all terms of order 0^2 and smaller, the electric field amplitudes for x and y polarizations at the entrance to the sensor are (listing the most significant term first)

$$E_{1x} = \cos^2(\theta_a) \cos(\theta_0) \{ [(1-\eta_f)(1-\eta_a)]^{1/2} e^{-i(\phi_f+\phi_a)} + [\eta_a(1-\eta_f)]^{1/2} [\tan(\theta_0) - \tan(\theta_a)] i e^{-i(-\omega_a t + \phi_a + \phi_f)} - (\eta_f \eta_a)^{1/2} e^{-i(\omega_a t + \phi_f)} - [\eta_a(1-\eta_f)]^{1/2} \tan(\theta_a) i e^{-i(\omega_a t + \phi_f)} \} |E_0| e^{i\omega t} \quad (44)$$

and the y electric field component

$$E_{1y} = \cos^2(\theta_a) \cos(\theta_0) \{ [\eta_a(1-\eta_f)]^{1/2} i e^{-i\omega_a t} + [\eta_f(1-\eta_a)]^{1/2} i e^{-i\phi_a} + [(1-\eta_f)(1-\eta_a)]^{1/2} \tan(\theta_a) e^{-i\phi_a} + [(1-\eta_f)(1-\eta_a)]^{1/2} [\tan(\theta_0) - \tan(\theta_a)] \} |E_0| e^{i\omega t} \quad (45)$$

To account for angular misalignment between the principal axes of the fiber and the principal stress axes of the sensor, both rotation θ_s and birefringent phase shift ϕ_s , due to the measurand, are included in the sensor Jones matrix.

$$\vec{E}_{2s} = S(\phi_s) R(\theta_s) \vec{E}_1 \quad (46)$$

where 2s indicates vector components along the sensor principal axes and $S(\phi)$ is the birefringent phase shift matrix

$$S(\phi) = \begin{vmatrix} 1 & 0 \\ 0 & e^{-i\phi} \end{vmatrix} \quad (47)$$

Instead of rotating back to the fiber axes, the intensity after the polarizer is more easily calculated in the sensor coordinate system, as shown in figure 11.

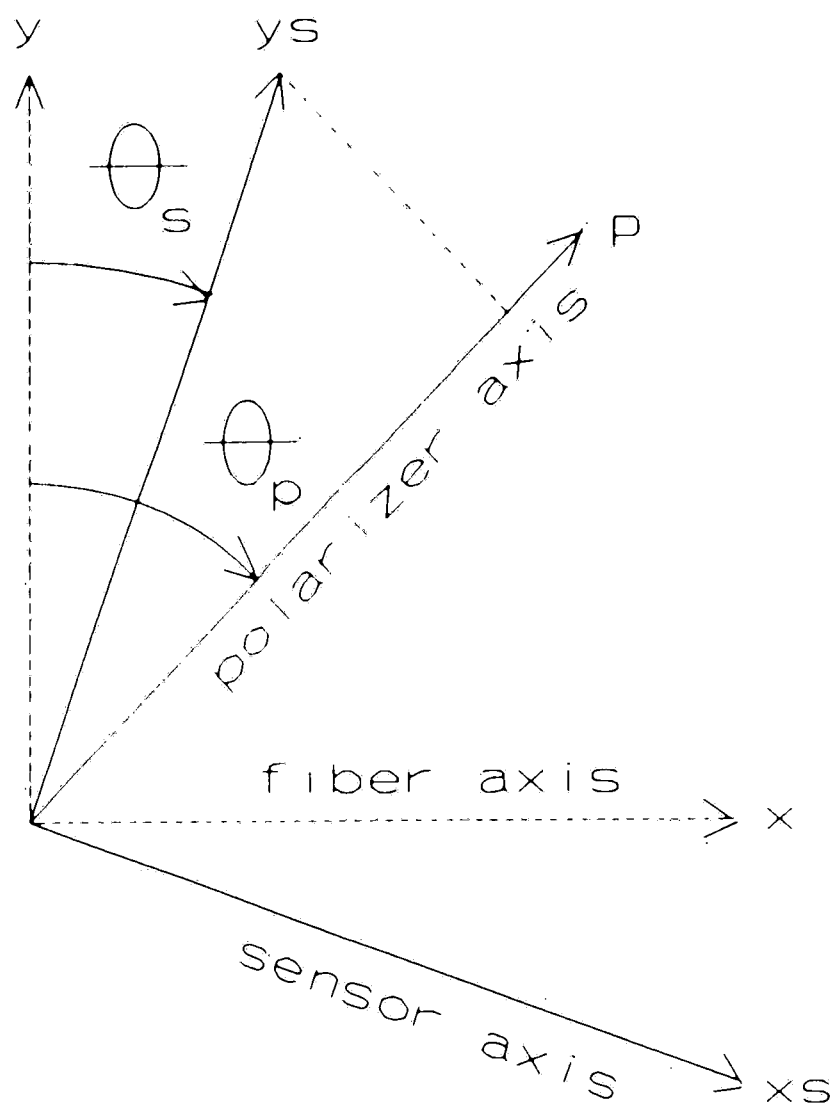


Figure 11. Electric field vector diagram at sensor exit polarizer

The light intensity passed by the polarizer, with polarization axis at angle θ_p , is then

$$I_3 = | E_{2sx} \text{SIN}(\theta_p - \theta_s) + E_{2sy} \text{COS}(\theta_p - \theta_s) |^2 \quad (48)$$

where the electric field vector after the sensor, in the sensor coordinate system is

$$\vec{E}_{2s} = \cos(\theta_s) \left| \begin{array}{l} E_{1x} + \tan(\theta_s) E_{1y} \\ [-\tan(\theta_s) E_{1x} + E_{1y}] e^{-i\phi_s} \end{array} \right| \quad (49)$$

Then the intensity after the polarizer in terms of E_{1x} and E_{1y} is given by equation 50.

$$I_3 = |E_0|^2 \cos^2(\theta_s) \left| (E_{1x} + \tan(\theta_s) E_{1y}) \sin(\theta_p - \theta_s) + e^{-i\phi_s} (-\tan(\theta_s) E_{1x} + E_{1y}) \cos(\theta_p - \theta_s) \right|^2 \quad (50)$$

I_3 consists of terms in $|E_{1x}|^2$, $|E_{1y}|^2$, $E_{1x}E_{1y}^*$, and $E_{1x}^*E_{1y}$. Some of these terms will create unwanted signal components at $2\omega_a$ and components without sensor phase dependence. These components can cause phase measurement errors in the differential heterodyne measurement. The major source of the $2\omega_a$ term is nonzero value of θ_0 . When both fiber polarization modes are excited, the resulting positive and negative frequency shifts are combined by the polarizer to produce $2\omega_a$ terms. To first order, the ratio of $2\omega_a$ and ω_a terms is equal to

$$\begin{aligned} I_3(\omega_a) &\propto E_0^2 \sqrt{\eta} \\ I_3(2\omega_a) &\propto E_0^2 \eta \theta_0 \\ \frac{I_3(2\omega_a)}{I_3(\omega_a)} &= \sqrt{\eta} \theta_0 \end{aligned} \quad (51)$$

The $2\omega_a$ term was reduced to negligible levels in these

experiments by accurate adjustment of θ_0 to zero.

η_f is theoretically equal to the h parameter of the polarization preserving fiber optic. Even though the measured fiber extinction ratio (1.6×10^{-3}) was greater than that predicted by the specified h value (10^{-5} /meter over 3 meters of fiber), η_f is still sufficiently small to be neglected. And since the polarization axis rotation, θ_a , calculated using equation 14, is only 2.2 milliradians for the experimental system, θ_a may also be neglected. If the error sources, η_f , θ_0 , and θ_a , are negligible, I_3 becomes

$$I_3 = |E_0|^2 \cos^2(\theta_s) (1 - \eta_f) [(1 - \eta_a) \eta_a]^{1/2} \{ \cos[2(\theta_e + \theta_s)] \sin(\omega_a t + \phi_f + \phi_a + \phi_s) - \sin(\theta_s) \sin[2(\theta_e + \theta_s)] \sin(\omega_a t + \phi_f + \phi_a) \} \quad (52)$$

where θ_e is the polarizer angular error from the nominal 45 degree orientation. The unwanted ω_a component, without sensor phase ϕ_s , is easily eliminated by careful alignment of the sensor principal axes and the polarizer ($\theta_s = 0$ and $\theta_e = 0$).

Noise and optical coherence

The phase measurement precision is limited by amplitude and phase noise. Phase measurement noise immunity depends upon the demodulation scheme: product demodulation, zero crossing measurements, or phase-locked loop. Due to the simplicity of flip/flop ECL circuitry, zero crossing measurements were demonstrated in this work. However, product demodulation should offer greater signal to noise due to the larger statistical sampling of the signal waveform.

The signals from detectors 1 and 2 (see figure 2) pass through two narrow band filters, whose pass bands are centered at the acoustic frequency, with bandwidth sufficient for the measurand. Two comparators hard limit these sinusoids producing two square waves separated by the time delay of the sensor birefringent phase shift. This time delay is measured by product demodulation, flip/flop phase discriminator, or precision counter. A flip/flop discriminator (see appendix A), which showed 0.1 milliradian phase stability at 2 Mhz, was constructed. But a high frequency counter was shown to be more reliable for experiments. Since the counter and flip/flop discriminator both measure zero crossing delay, the noise analysis is identical for both cases.

Laser amplitude and phase noise, detector noise, and voltage offsets are the major contributors to system errors. The effects of the laser noise are included by changing equation 7 to the following form

$$\begin{aligned} E_x &= A_x(t) \cos\left[\left(\omega_x + \delta\omega(t)\right)\left(t - \frac{n_x l_x}{c_0}\right)\right] \\ E_y &= A_y(t) \cos\left[\left(\omega_y + \delta\omega(t)\right)\left(t - \frac{n_y l_y}{c_0}\right)\right] \end{aligned} \quad (53)$$

where n_x and l_x are the refractive index and physical path length for the x polarization, and likewise for y. $A(t)$ is the amplitude of the laser diode and $\delta\omega(t)$ is the phase or frequency variation. The intensity measured by each detector, $j=1$ or 2 (see figure 2), is then

$$\begin{aligned} \langle I_j \rangle &= \langle E_{xj}^2 + E_{yj}^2 \rangle \\ &= \frac{1}{2} (I_{xj} + I_{yj}) + \sqrt{I_{xj} I_{yj}} \cos[Q(t)] \end{aligned} \quad (54)$$

where the phase $Q(t)$ of the heterodyne term is

$$Q_j(t) = (\omega_x - \omega_y) t - \frac{\omega_x n_{xj} l_{xj}}{c_0} + \frac{\omega_y n_{yj} l_{yj}}{c_0} - \delta\omega(t) \left(\frac{n_{xj} l_{xj}}{c_0} - \frac{n_{yj} l_{yj}}{c_0} \right) \quad (55)$$

and where the intensities consist of a zero frequency component I_0 and amplitude noise I_{0n} .

$$\begin{aligned} I_{xj} &= I_{0xj} + I_{0nxj}(t) \\ I_{yj} &= I_{0yj} + I_{0nyj}(t) \end{aligned} \quad (56)$$

The signal voltage after passing through a narrowband filter with center frequency ω_a is

$$\begin{aligned} V_j &= R_j I_{nj} + R_j \sqrt{I_{xj} I_{yj}} \cos[Q(t)] + V_{nj}(t) + V_{0j} \\ I_{nj} &= \frac{1}{2} (I_{nxj} + I_{nyj}) \end{aligned} \quad (57)$$

where R_j is the product of detector responsivity and gain, I_{nj} and V_{nj} are the laser amplitude noise and detector output noise, respectively, which are passed by the narrowband filter. V_{0j} is the difference between the signal voltage offset and the comparator threshold level. Since this threshold is usually near zero, $\cos(Q(t))$ may be approximated by $Q(t) - \pi/2$. Then the time when the signal crosses the comparator threshold, at zero volts, is

$$t_j = \frac{1}{\omega_a} \left(\Delta\phi_j + \frac{\pi}{2} - \frac{R_j I_{nj} + V_{nj}(t) + V_{0j}}{R_j \sqrt{I_{xj} I_{yj}}} \right) \quad (58)$$

where the birefringent phase in the channel j (sensor or reference detector) is

$$\Delta\phi_j = \phi_{xj} - \phi_{yj} \quad (59)$$

Then the time delay between zero crossings of the two signals is

$$\Delta t = \frac{1}{\omega_a} \left(\Delta\phi_1 - \Delta\phi_2 - \frac{V_{n2}(t) - V_{n1}(t) + V_{02} - V_{01}}{R\sqrt{I_x I_y}} \right) \quad (60)$$

where we assume that the channel gains are adjusted to equalize the amplitudes of the heterodyne signals and therefore cancel the noise contributions due to the correlated laser amplitude noise components in each channel.

$$R\sqrt{I_x I_y} = R_1\sqrt{I_{x1} I_{y1}} = R_2\sqrt{I_{x2} I_{y2}} \quad (61)$$

Assuming V_{n1} and V_{n2} to be uncorrelated gaussian random processes, the standard deviation of the delay time for N_t successive measurements of Δt becomes

$$\sigma_{\Delta t} = \frac{[\langle V_{n1}^2(t) \rangle + \langle V_{n2}^2(t) \rangle]^{1/2}}{\sqrt{N_t} \omega_a R \sqrt{I_x I_y}} \quad (62)$$

with static phase error due to voltage offsets

$$\Delta\phi_0 = \frac{V_{01} - V_{02}}{\omega_a R \sqrt{I_x I_y}} \quad (63)$$

The mean of the squared noise voltage depends upon the power spectral density of the noise, $P_n(\omega)$, and the transfer function of the narrowband filter, $H_f(\omega)$.

$$\langle V_{nj}^2(t) \rangle = \int_{-\infty}^{\infty} P_{nj}(\omega) H_f(\omega) d\omega \quad (64)$$

Since the noise power spectral density is flat across the filter bandwidth, $\Delta\omega_f$, we may approximate the rms noise by $P(\omega_a)\Delta\omega_a$. The number of measurements, N_t , equals $\omega_a T_m / 2\pi$, where T_m is the total measurement time. Substituting these terms and the mode coupling efficiency, η , into equation 64 we obtain

$$\sigma_{\Delta t} = \frac{1}{R \omega_a^{3/2}} \left(\frac{2\pi [P_{n1}(\omega_a) + P_{n2}(\omega_a)] \Delta\omega_f}{T_m \eta (1 - \eta) (I_x + I_y)} \right)^{1/2} \quad (65)$$

The time delay standard deviation may be reduced by decreasing the noise and filter bandwidth or by increasing the measurement time and acoustic frequency. However, ω_a is limited by the speed of the phase discriminator electronics.

In addition to the amplitude noise, equation 55 indicates a source phase noise term given by equation 66

$$\begin{aligned} \delta\phi &= \frac{\delta\omega(t)}{c_0} (n_x l_x - n_y l_y) \\ \delta\phi &= \frac{-\delta\lambda}{\lambda} (\phi_x - \phi_y) \end{aligned} \quad (66)$$

The phase noise in signals 1 and 2 is proportional to the birefringence in paths 1 and 2. For polarization preserving

fiber, the birefringent phase accumulates at 2π per beat length. The resulting phase noise is negligible for most gas lasers due to the enormous Q of the laser cavity. But as demonstrated by Dandridge, et al (31) the phase noise of laser diodes is typically much larger than for gas lasers. The wavelength noise of a Hitachi 1400 CSP laser ($\lambda = 830$ nm) is listed below at various frequencies:

Frequency (Hz)	$\delta\lambda$ (nm)/ $\sqrt{\text{Hz}}$	δf (KHz)/ $\sqrt{\text{Hz}}$
50	1.6×10^{-7}	70
100	1.0×10^{-7}	43
2000	1.0×10^{-8}	4.3

For example, at 50 Hz the phase noise equals $0.6 \mu\text{rad}/\sqrt{\text{Hz}}$ per meter of optical fiber, with 2 mm beat length. Since the noise level increases as $1/\sqrt{f}$, this noise may become significant at low frequencies. But the differential phase measurement eliminates the noise due to fiber optical path difference, leaving only the noise due sensor birefringence which is negligible.

Another source of phase noise is temperature drift of the laser diode wavelength (approximately $0.23 \text{ nm}/^\circ\text{C}$). This drift causes an enormous phase drift of $0.85 \text{ rad}/^\circ\text{C}$ per meter of fiber (2 mm beat length). The differential heterodyne measurement eliminates the common mode phase drift due to the fiber optic optical path difference, resulting in a residual phase error of $0.028 \text{ } \%/^\circ\text{C}$ of the measured sensor phase shift. Even for short lengths of

polarization preserving fiber, this measurement would not be possible without differential heterodyne. The differential phase measurement eliminates the need for laser diode temperature control.

One other related consideration is laser diode coherence length. The polarization preserving fiber accumulates optical path difference (OPD) between the polarization modes as described by

$$OPD = \frac{\lambda l_f}{n_f L_b} \quad (67)$$

where l_f and n_f are the total length and core refractive index of the fiber. For a 2 mm beat length, OPD accumulates at 0.28 mm per meter of fiber, at $\lambda = 830$ nm. The analysis so far has assumed an interference visibility of 1.0, requiring a coherence length much longer than the OPD. Even small amounts of backreflected light, due to Fresnel reflections and scattering, will significantly shorten the laser diode coherence length. Miles, et al, (32) measured the optical bandwidth of an 830 nm laser diode with various amounts of optical feedback. The approximate bandwidth and coherence length, which are related by $l_c = c/\Delta f$, are listed below.

Feedback (%)	Linewidth (Ghz)	l_c (mm)
0.2	1	300
0.3	6.0	50
1.0	6.4	47
10.0	11.4	26

For 10 meters of polarization preserving fiber, the OPD will be approximately 2.5 mm, resulting in 0.5 heterodyne visibility with 10% feedback. So for longer fiber lengths, either optical isolation or angled fiber ends with antireflection coatings are required to reduce the feedback.

Experimental system design

The basic concept of differential heterodyne was demonstrated using a HeNe gas laser with coherence length greater than 100 mm. This choice was supported by the availability of waveplates, polarizers, beamsplitters, and polarization preserving fiber optic at the 632.8 nm wavelength of HeNe. The experimental optical system (see figure 12) consists of a 3 mW HeNe laser source, 3 meters of polarization preserving fiber optic (beat length = 1.61 mm), 2 polarizers, and a thin film cube beamsplitter.

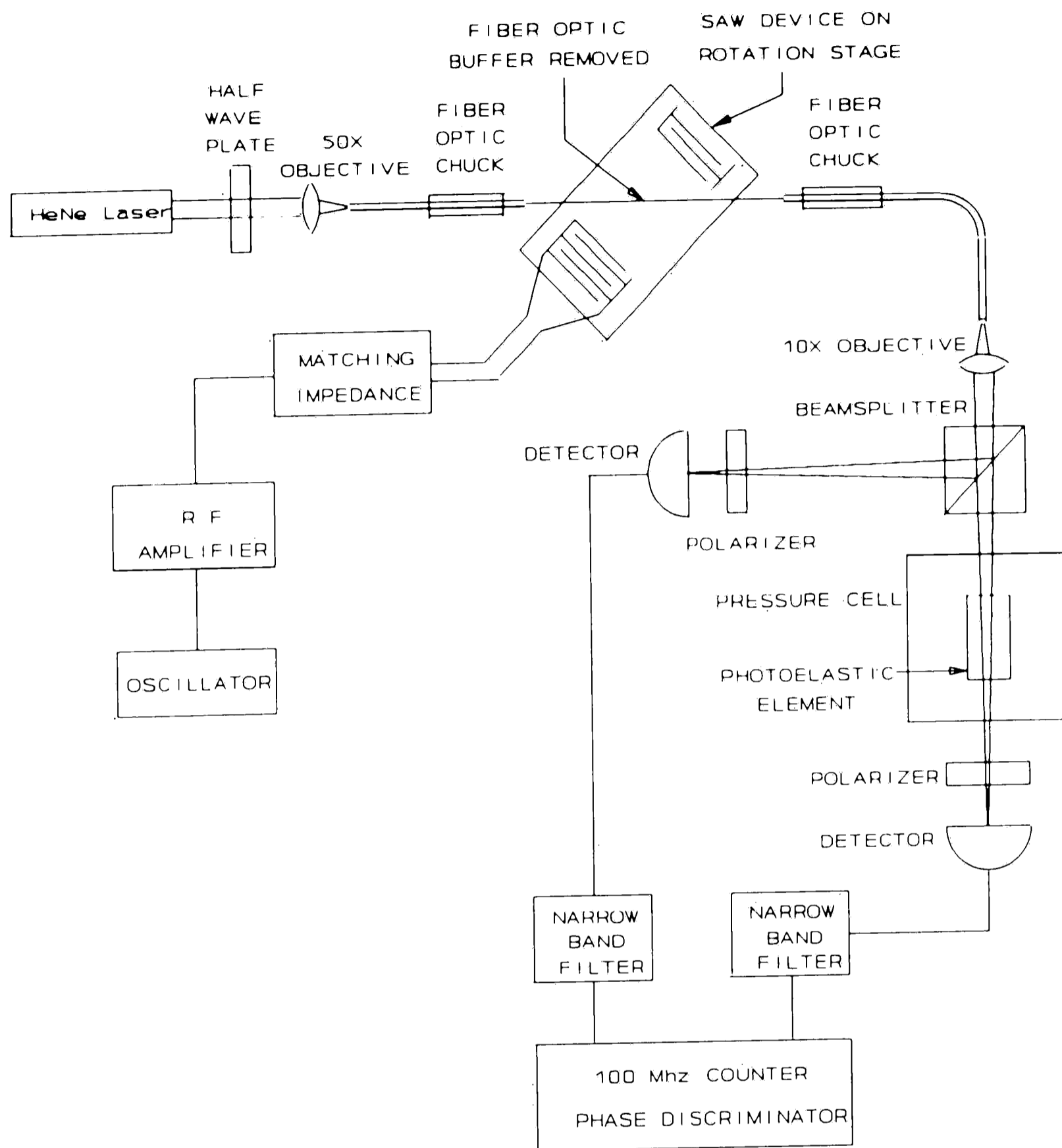


Figure 12. Experimental system

The fiber was chosen to have very low beat length temperature dependence ($0.02\%/^{\circ}\text{C}$), so as to maintain phase matching in the frequency shifter in spite of the 25°C change in SAW substrate temperature during warmup.

The fiber was 3M type FS-HB-3611, with 3.3 micron mode field diameter, 80 micron cladding diameter, and a 1.61 mm beat length at the 633 nm wavelength.

After passing through a half-wave plate, the HeNe laser beam is focused by a 50X microscope objective into the fiber optic. The fiber is supported by micrometer mounts with the submicron stability required to maintain alignment into the 3 micron fiber core. Coupling efficiency into the fiber was 34%. The polarization orientation at the fiber is adjusted by rotating the half wave plate while measuring the polarization extinction at the fiber exit. The extinction is most easily maximized with a spinning polarizer, by adjusting for the largest modulation. Maximum extinction was 1.65×10^{-3} .

The fiber is suspended, by two low stress fiber chucks, across the SAW device at an angle to optimize phase matching. The fiber buffer was stripped with methylene chloride to provide direct glass to ceramic contact on the SAW device. The output of the fiber is collimated by a 10X microscope objective and is split into two beams by a thin film beamsplitter. The thin film cube beamsplitter preserves the relative amplitudes of the two polarizations, adding only a small constant phase shift.

One beam passes through a polarizer to a silicon photodetector (UDT 455HS) to create the reference heterodyne signal. And the second beam passes through the optical stress sensor, which is stressed by a steel cylinder under pressure from a tank of nitrogen. This pressure was monitored by an electronic pressure sensor.

Each of these two heterodyne signals pass through a positive feedback active narrowband filter as described in the appendix B. These filters were centered at 1.97 Mhz, with a Q of 15 (133 Khz FWHM) and a gain of 60. The signals are monitored by an analog scope and a 100 MHz counter which is capable of 0.1 nsec delay measurements with a 15 second integration time.

The SAW device was created by photolithography on a PZT-4 substrate of dimensions 50mm wide, 78mm long, and 10mm thick. The large thickness reduces reflections of bulk acoustic waves from the bottom of the substrate. The top surface was chemically polished to submicron roughness and sputtered with a 1 micron thick layer of aluminum. After coating with photoresist, the substrate was exposed through the photomask shown, in figure 13, and then etched to leave interdigitated finger patterns for both the SAW transmitter and receiver.



Figure 13. Photomask of the SAW interdigitated finger pattern

The finger pattern contains 19 fingers in the transmitter and 5 fingers in the receiver, all with width and spacing of 0.27 mm. The resulting 1.08 mm acoustic wavelength and 20 mm acoustic aperture provides phase matching over the range of common beat lengths, from 1.1 mm to 2.0 mm, by adjusting the fiber angle. For the 1.61 beat length here, the angle between the fiber and the acoustic propagation direction is 47.9 degrees. The fiber is supported on an optical table, and the SAW device is mounted on a rotating stage. The stage is roughly adjusted to the optimum angle (within 0.5°) and then any residual phase mismatch is eliminated by tuning of the acoustic frequency. Acoustic absorbing material, plasticine, was placed on the ends of the substrate to

reduce acoustic reflections.

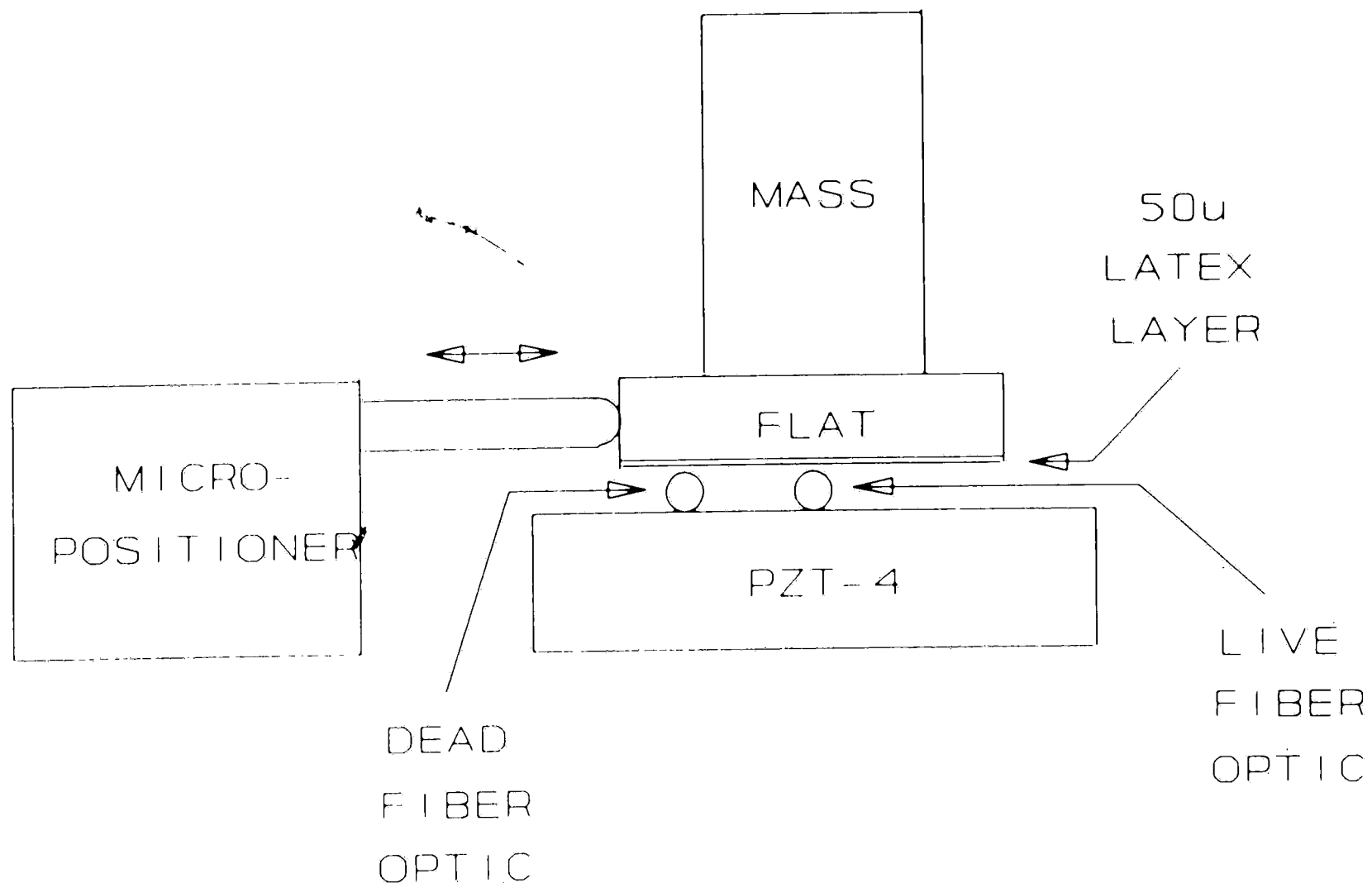


Figure 14. Structure for maintaining contact between the fiber optic and SAW substrate

Due to the small surface acoustic wave amplitude, good contact between the fiber and SAW substrate is crucial. Also the fiber principal polarization axes must be oriented near 45° with respect to the SAW plane for optimum mode coupling. These requirements were satisfied by the configuration shown in figure 14. A sheet of 50μ thick latex (condom) is stretched over a glass flat. The latex provides even pressure over the entire fiber. A 200 gm mass compresses the active fiber and a second short piece of

fiber between the glass flat and the substrate. The angle of the fiber principal axes is adjusted by pushing the glass flat with a glass rod, attached to a micrometer stage, thereby rolling the fibers on the substrate. With this system, complete tuning is accomplished in seconds.

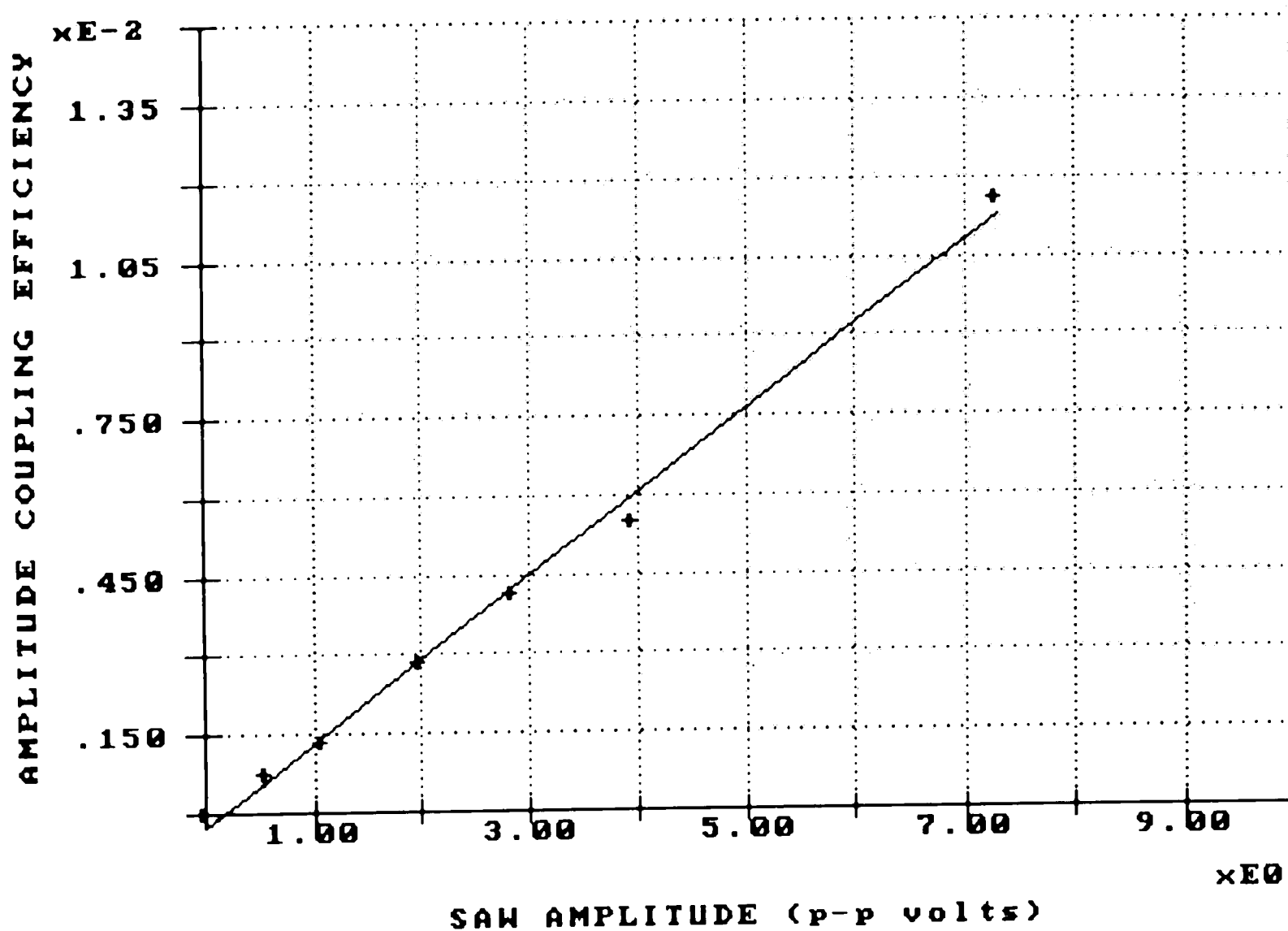


Figure 15. Electric field mode coupling efficiency vs. SAW amplitude

The mode coupling efficiency, was measured as a function of the acoustic wave amplitude as indicated by the SAW receiver. Figure 15 shows the coupling efficiency, η , vs. peak to peak SAW receiver voltage amplitude. At these low

efficiencies, the coupling efficiency is proportional to the acoustic amplitude, in agreement with theory. Even though the coupling efficiency is only 1%, the narrowband filter provides excellent signal to noise because all of the measurand signal is in a very narrow frequency band centered on the acoustic frequency.

Differential Phase Experiments

The primary goal of this work is to demonstrate a differential heterodyne sensor using a surface acoustic wave mode coupler. Pressure sensing was demonstrated with two optical materials, fused silica and Lexan (polycarbonate). Blocks of these materials, with polished ends, were prepared in 2.54 cm lengths. The block crosssections were 0.56x0.63cm and 0.32x0.63cm for the polycarbonate and silica, respectively. In each case, the sample was compressed by a 2.22cm diameter steel cylinder, driven by compressed nitrogen. An electronic pressure transducer monitored the cylinder force while the differential phase delay was measured with a counter. Using the ratio of crosssectional areas of the blocks and the steel cylinder, the stress in the blocks was determined. The internal differential stress, S , is related to the principal strains, S_{xx} and S_{yy} , by

Young's modulus (modulus of elasticity), χ , and Poisson's ratio, σ .

$$S = \chi(S_{xx} - S_{yy}) = \chi(1 + \sigma)S_{xx} \quad (68)$$

Poisson's ratios for silica and polycarbonate are 0.17 and 0.38, respectively.

Then, using equation 6, the differential stress optic coefficient, C_o , is

$$C_o = \frac{n^3}{2\chi}(P_{11} - P_{12}) \quad (69)$$

The birefringent phase shift in the block is

$$\phi_x - \phi_y = \frac{2\pi(1 + \sigma)C_o Z S}{\lambda} \quad (70)$$

where Z is the optical propagation distance in the stressed block.

The plots of differential delay, between the two heterodyne signals, vs. calculated stress are shown in figures 16 and 17. The experimental data is plotted along with a least squares linear fit. Both data sets show good linearity as expected.

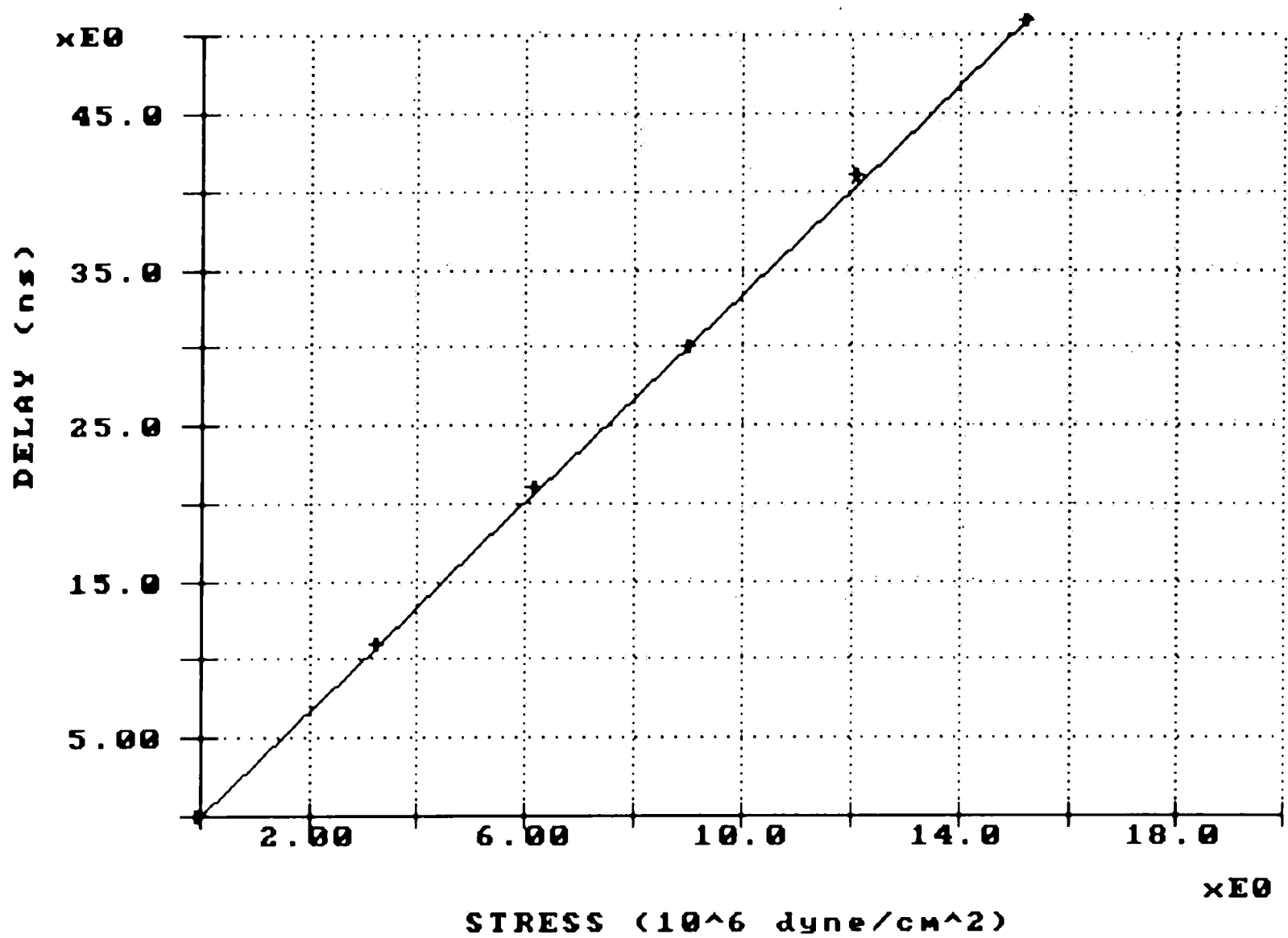


Figure 16. Differential heterodyne phase delay vs. stress for silica sensor element

The differential stress optic coefficient is related to the slope in figures 16 and 17 by

$$C = \frac{\lambda \Delta t}{(1 + \sigma) Z T_0 S} \quad (71)$$

where T_0 is the period of the heterodyne signal. The following table lists the slopes for both experiments and the corresponding stress optic coefficients.

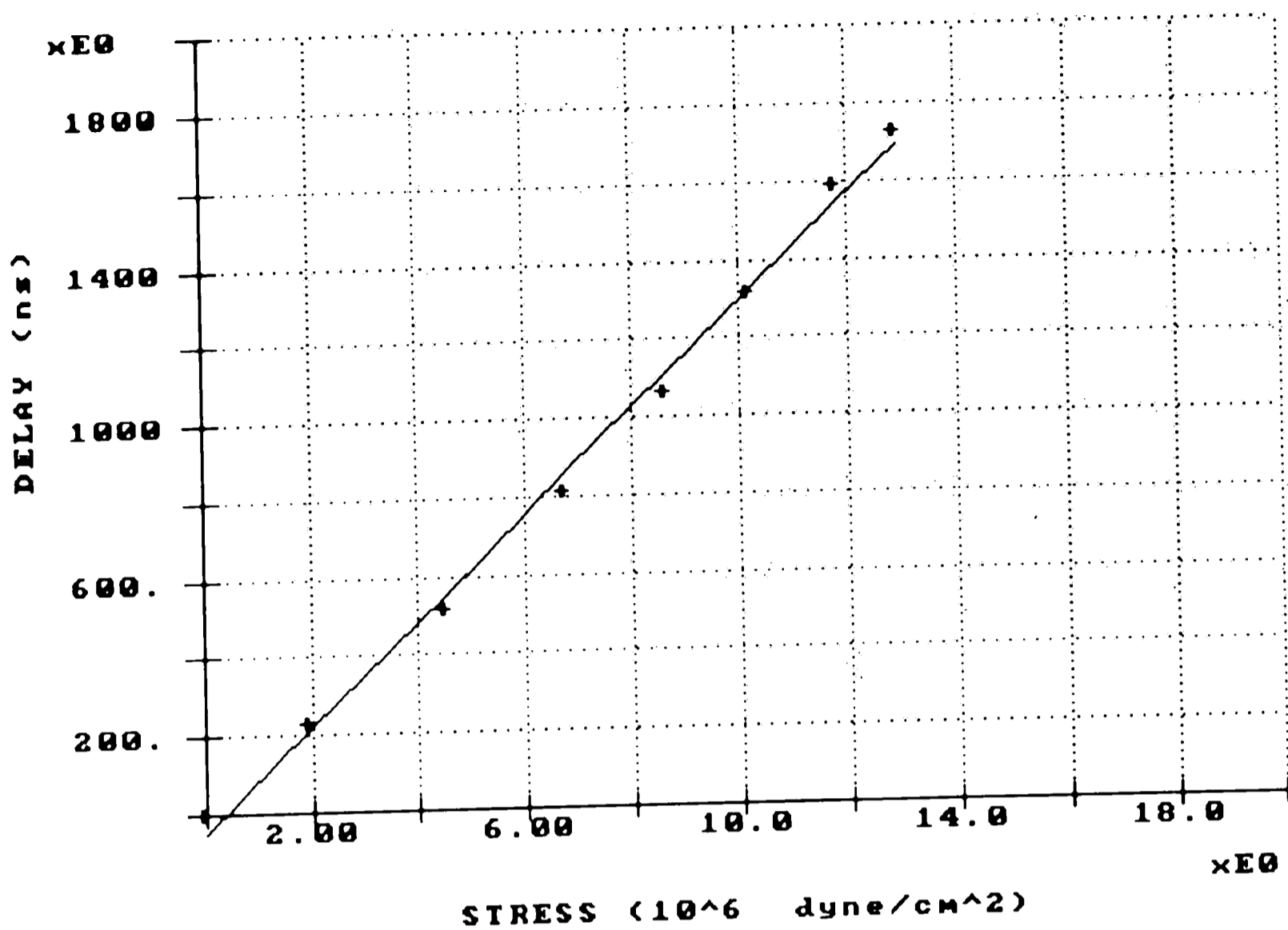


Figure 17. Differential heterodyne phase delay vs. stress for polycarbonate sensor element

	$\Delta t/S$ (10^{-6} ns cm ² /dyne)	$C_0(\text{exp})$ (10^{-13} cm ² /dyne)	$C_0(\text{lit})$ (10^{-13} cm ² /dyne)
Silica	3.34	1.33	3.30
Lexan	135	45.4	74

$C_0(\text{exp})$ is the differential stress optic coefficient calculated from experiment and $C_0(\text{lit})$ is the coefficient found in the literature, see references (33) for

polycarbonate and (34) for silica. Due to optical inhomogeneities and property variation among manufacturers, the agreement between $C_o(\text{exp})$ and $C_o(\text{lit})$ for polycarbonate is acceptable. However, silica is very well characterized and better agreement would be expected. After the experiments, a small chip was missing from the edge of the silica element, indicating a possible misalignment between the compression cylinder and the silica surfaces. Therefore, the stress field inside the element was probably not uniform, causing a decrease in the calculated stress optic coefficient. The nonuniform stress field still shows good linearity between heterodyne delay and stress, as expected.

The pressure cell was replaced by a quarter wave plate ($\lambda=632.8$ nm) to verify the absolute birefringent phase accuracy. The results are shown below.

Quarter Wave Plate (0.25λ)

T_0 (ns)	Δt (ns)	phase shift
540	132 \pm 4	0.244 \pm .007 λ

The measured delay of 132 ns, instead of 135 ns for quarter wave, is within the specified accuracy of 0.01λ for the waveplate.

Another experiment was performed to demonstrate that the heterodyne signal does not depend upon optical spatial coherence after the polarizers. The reference and sensor

beams were focussed into multimode fiber optics, which were each coupled to a silicon detector. Since the heterodyne signals were preserved through the multimode fiber optics, the complete configuration, including the loss of spatial coherence in the multimode fibers, was demonstrated.

Conclusion

A differential heterodyne polarimetric sensor, using a surface acoustic wave frequency shifter and HeNe laser, was demonstrated. Stress induced birefringence, in silica and polycarbonate, and a mica waveplate were measured to demonstrate the measurement of birefringent phase delay. Analysis of a diode laser based sensor predicts equivalent performance, without the need for laser diode temperature control. Also coherence length and laser phase noise should not be a problem in laser diode systems, for fiber lengths less than 20 meters.

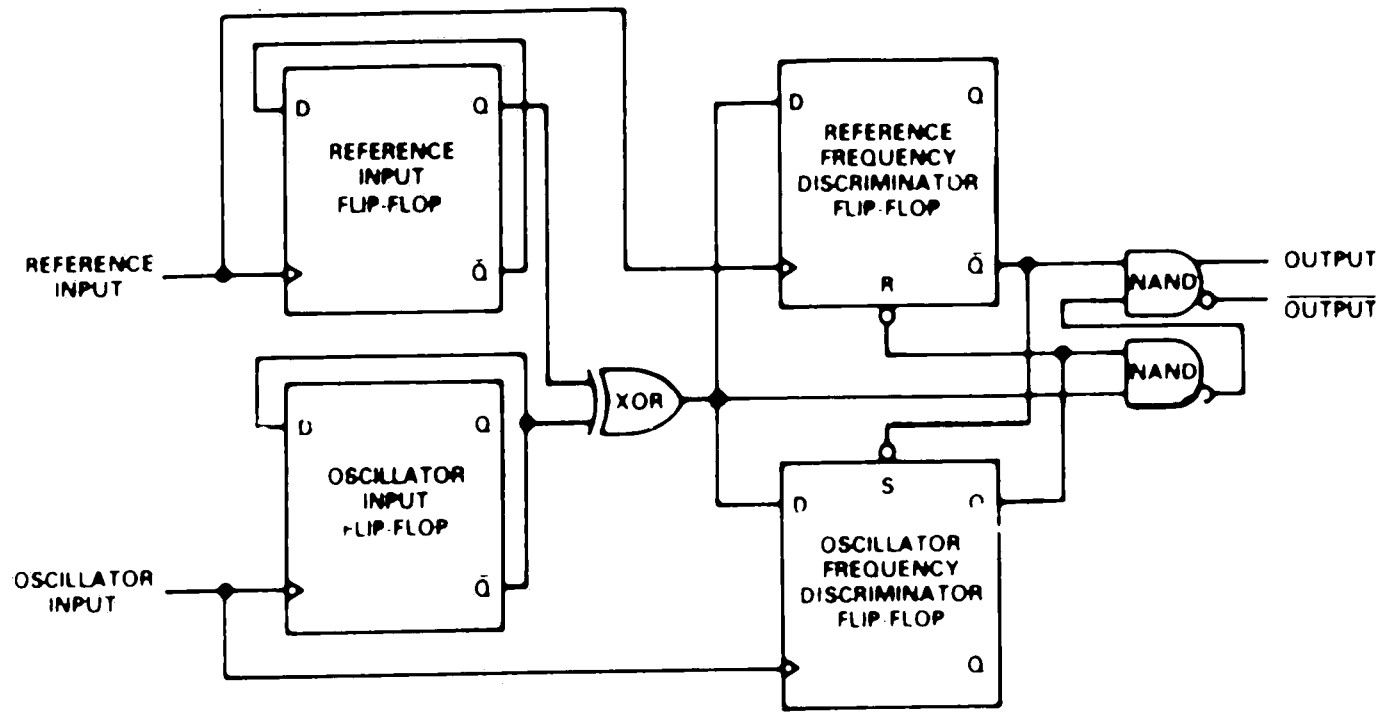
REFERENCES

- (1) Giallorenzi, T.G., et al, Optical Fiber Sensor Technology, IEEE J. Quantum Electronics, Vol. QE-18, No. 4, pp 626-665, April 1982
- (2) Johnson, L. and Jensen, S., "Problems and Approaches for Remote Fiber Optic Absolute Sensors", Proceedings of SPIE conference: Fiber Optic and Laser Sensors III, SPIE Vol. 566, p.45, 1985
- (3) Iizuka, K., Engineering Optics. 2nd ed., p.397, Springer-Verlag, 1987
- (4) Yamamoto, Y. and Kimura, T., "Coherent Optical Fiber Transmission Systems," IEEE J. Quantum Electron., Vol. QE-17, pp. 919-935, June 1981
- (5) Peng, G., Huang, S., and Lin, Z., "A New Heterodyne Fiber Optic Gyroscope Using Electrooptic Frequency Shifter" J. Lightwave Technol., Vol. LT-5, No.7, pp 986-989, July 1987
- (6) Giles, I., Culshaw, B., and Davies, D., " Heterodyne Optical Fiber Gyroscope", First International Conference on Optical Fibre Sensors, IEE No. 221 pp 151-154, April 1983
- (7) J. Jones, M. Corke, A. Kersey and D. Jackson, " Laser Diode Frequency Modulation for Directional Laser Doppler Velocimeter", *ibid*, pp 178-181
- (8) D. Uttam, I. Giles, B. Culshaw, and D. Davies, " Remote Interferometric Sensors using Frequency Modulated Laser Sources", *ibid*, pp 182-184
- (9) B. Culshaw and I. Giles, "Frequency Modulated Heterodyne Optical Fiber Sagnac Interferometer", IEEE J. Quantum Electron., Vol. QE-18 No.4 , pp 690-693, April 1982
- (10) H. Ghafoori-Shiraz and T. Okoshi, " Fault Location in Optical Fibers using Frequency Domain Reflectometry", J. Lightwave Technol. Vol. LT-4, No. 3, pp 316-321, March 1986

- (11) S. Kingsley, " OFDR Diagnostics for Fiber/Integrated Optic Systems and High Resolution Distributed Fiber Optic Sensing", Proceedings of SPIE Conference: Fiber Optic and Laser Sensors III, Vol. 566, pp 265-275, August 1985
- (12) A. Yariv, " Optical Electronics ", Chapter 12, 1985
- (13) S. Kobayashi, Y. Yamamoto, M. Ito and T. Kimura, " Direct Frequency Modulation in AlGaAs Semiconductor Lasers", IEEE J. Quantum Electron., Vol. QE-18 No.4, pp. 582-595, April 1982
- (14) A. Dandridge and L. Goldberg, " Current-induced Frequency Modulation in Diode Lasers ", Electronics Lett. Vol.18 No.7, pp 302-304, April 1982
- (15) D. Welford and S. Alexander, " Magnitude and Phase Characteristics of Frequency Modulation in Directly Modulated GaAlAs Semiconductor Diode Lasers ", J. of Lightwave Technol., Vol. LT-3 No.5 pp 1092-1099, Oct.1985
- (16) K. Wong, R. De La Rue, and S. Wright, " Electro-optic-waveguide Frequency Translator in LiNbO3 Fabricated by Proton Exchange ", Optics Lett. Vol.7 No.11, pp 546-548 November 1982
- (17) K. Nosu, S. Rashleigh, H. Taylor, J. Weller, " Acousto-Optic Frequency Shifter for Single-Mode Fibres", Electronics Lett. Vol. 19 No.20, pp 816-818, Sept. 1983
- (18) W. Risk, R. Youngquist, G. Kino, H. Shaw, " Acousto-Optic Frequency Shifting in Birefringent Fiber", Optics Lett. Vol.9 No.7, pp 309-311, July 1984
- (19) W. Risk, R. Youngquist, G. Kino, H. Shaw, " Single-Sideband Frequency Shifting in Birefringent Optical Fiber", Proceedings of SPIE Conference: Fiber Optic and Laser Sensors II, Vol. 478, pp 91-97
- (20) W. Risk, G. Kino, H. Shaw, " Fiber-optic Frequency Shifter Using a Surface Acoustic Wave Incident at an Oblique Angle", Optics Lett. Vol.11, No.2, pp 115-117, Feb. 1986
- (21) W. Risk and G. Kino, " Acousto-optic Fiber-optic Frequency Shifter Using Periodic Contact With a Copropagating Surface Acoustic Wave", Optics Lett. Vol.11, No.5 pp 336-338, May 1986
- (22) Greenhalgh, P., Foord, A., and Davies, P., "All-fibre Frequency Shifter Using Piezoceramic SAW Device", Elect. Lett. Vol. 25 No. 18 p.1206, 31 Aug. 1989

- (23) R. Youngquist, J. Brooks, and H. Shaw, "Birefringent-Fiber Polarization Coupler", Optics Lett. Vol. 8 No. 12 pp 656-658, December 1983
- (24) A. Yariv, "Coupled-Mode Theory for Guided-Wave Optics", IEEE J. Quantum Electronics, Vol. QE-9, No.9, pp 919-933 September 1973
- (25) Datta, S., "Surface Acoustic Wave Devices", Prentice-Hall N.J., 1986
- (26) Campbell, C., "Surface Acoustic Wave Devices and Their Signal Processing Applications", Academic Press, 1989
- (27) Matthews, H., "Surface Wave Filters: Design, Construction, and Use", John Wiley & Sons N.Y., 1977
- (28) Marton, L., "Methods of Experimental Physics: Ultrasonics", p.54, Academic Press, 1981
- (29) Rashleigh, S., "Origins and Control of Polarization Effects in Single-mode Fibers", J. Lightwave Technology, Vol.LT-1 No.2, p.312, June 1983
- (30) Risk, W., "Fiber-optic Modulators Using Acoustically-Induced Polarization Coupling", internal memorandum G.L. No. 4066, Edward L. Ginzton Laboratory, Stanford University, June 1986
- (31) Dandridge A., Tveten A., Miles, R., Jackson, D., and Giallorenzi, T., "Single-mode Diode Laser Phase Noise", Appl. Phys. Lett., Vol. 38 No.2, p.77, 15 Jan. 1981
- (32) Miles, R., Dandridge, A., Tveten, A., Taylor, H., Giallorenzi, T., "Feedback-induced Line Broadening in CW Channel-substrate Planar Laser Diodes", Appl. Phys. Lett., Vol. 37 No. 11, 1 Dec. 1980
- (33) Agarwal, R. and Teufel, L., "Epon 828 Epoxy: a New Photoelastic-model Material", Experimental Mechanics, p.30, March 1983
- (34) Borrelli, N. and Miller, R., "Determination of the Individual Strain-optic Coefficients of Glass by an Ultrasonic Technique", Applied Optics Vol.7 No.5, p.745, May 1968
- (35) Analog Devices, specification sheet for ultrahigh speed phase/frequency discriminator, AD9901
- (36) Johnson, D. and Hilburn, J., "Rapid Practical Designs of Active Filters", p.156, John Wiley & Sons N.Y. 1975

Appendix A



AD9901 Block Diagram

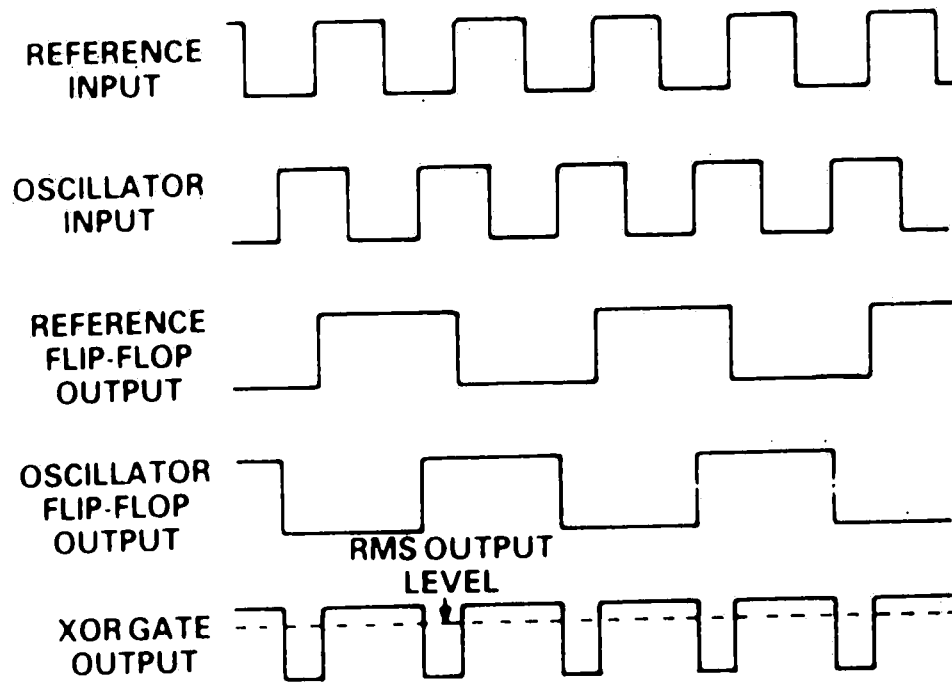


Figure 18. Phase Discriminator

Appendix B

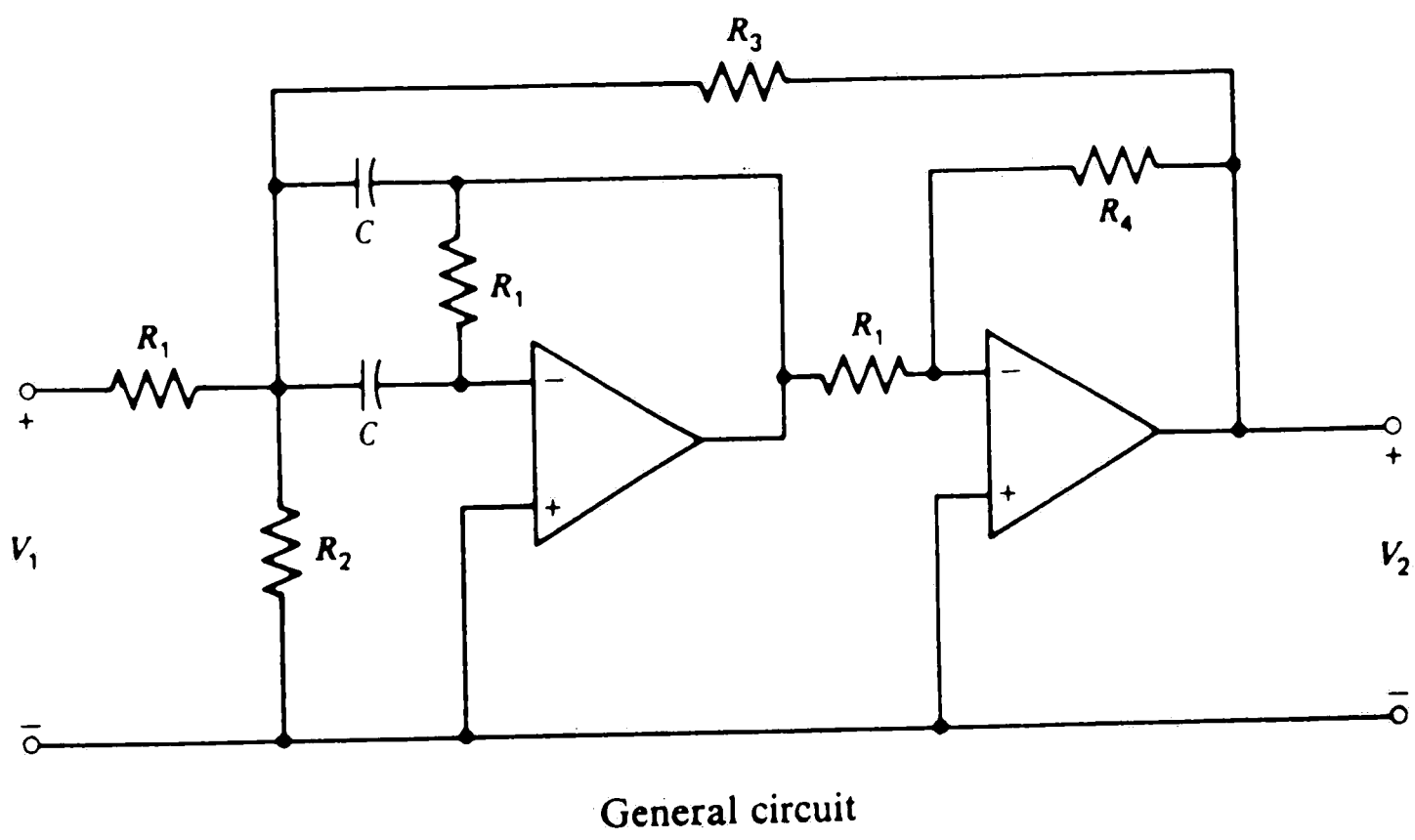


Figure 19. Positive-feedback active bandpass filter

Vita

Michael N. Trainer
186 Fretz Road
Telford, Pa. 18969

Education:

B.S. Engineering Physics	Lehigh University	1973
M.S. Optics	University of Rochester	1976

Employment History:

1976 - present	Corporate Research Leeds & Northrup North Wales, Pa. 19454
----------------	--

Principal Scientist

Conducted the development of fiber optic sensors, optical data storage systems, and optical instrumentation for size analysis of small particles, using photon correlation and angular light scattering.